Understanding Multi-Ion Transport Mechanisms in Bipolar Membranes

Justin C. Bui[1,2], Ibadillah Digdaya[3], Chengxiang Xiang[3], Alexis T. Bell[1,2], and Adam Z. Weber[2]*

[1] Department of Chemical and Biomolecular Engineering
University of California Berkeley
Berkeley, CA 94720, USA

[2] Joint Center for Artificial Photosynthesis
Lawrence Berkeley National Laboratory
Berkeley, CA 94720, USA

[3] Joint Center for Artificial Photosynthesis
California Institute of Technology
Pasadena, CA 91125, USA

***Corresponding Author**
email: azweber@lbl.gov
phone: (510) 486-6308

Bipolar membranes (BPMs) have the potential to become critical components in electrochemical devices for a variety of electrolysis and electrosynthesis applications. Because they can operate under large pH gradients, BPMs enable favorable environments for electrocatalysis at the individual electrodes. Critical to the implementation of BPMs in these devices is understanding the kinetics of water dissociation that occurs within the BPM as well as the co- and counter-ion crossover through the BPM, which both present significant obstacles to developing efficient and stable BPM-electrolyzers. In this study, a continuum model of multi-ion transport in a BPM is developed and fit to experimental data. Specifically, concentration profiles are determined for all ionic species, and the importance of a water dissociation catalyst is demonstrated. The model describes internal concentration polarization and co- and counter-ion crossover in BPMs, determining the mode of transport for ions within the BPM and revealing the significance of ion crossover when operated with pH gradients relevant to electrolysis and electrosynthesis. Finally, a sensitivity analysis reveals that the performance and lifetime of BPMs can be improved substantially by using of thinner dissociation catalysts, managing water transport, modulating the thickness of the individual layers in the BPM to control salt-ion crossover, and increasing the ion-exchange capacity of the ion-exchange layers in order to amplify the water dissociation kinetics at the interface.

Keywords: bipolar membrane, transport, model, electrochemistry, ionomers, electrolysis, CO_2 reduction, water splitting

1. Introduction

As electricity from renewable sources becomes less expensive and more prevalent, the electrochemical conversion of low-value feedstocks to high-value products (electrolysis or electrosynthesis) will become a key means for storing excess electrical energy in chemical carriers, simultaneously offsetting the intermittency of renewable energy sources and decarbonizing various sectors of the economy.[1–3] Recently, engineering studies have focused on developing devices that can perform these electrochemical reactions with high energy efficiency. This has led to the adoption of a membrane-electrode-assembly (MEA) architecture, which exhibits reduced ohmic losses relative to those occurring in a liquid-electrolyte cell.[4–7]

In an MEA architecture, the acidity of alkalinity of the ion-exchange membrane dictates the pH for the electrochemical reactions occurring in the device. Anion-exchange membranes (AEMs) necessitate alkaline pHs at both electrodes. Similarly, cation-exchange membranes (CEMs) necessitate acidic pHs at both electrodes. This is unfortunate because, for many electrolysis or electrosynthesis reactions, the optimal conditions for the anode catalyst occur in a drastically different pH environment than that for the cathode catalyst.[8–12] Therefore, many electrochemical reactions could benefit from operation under a pH gradient.

Consider the electrolysis of water to hydrogen (H_2) and oxygen (O_2)—a relatively simple electrochemical reaction that has been heavily studied due to hydrogen's particular attractiveness as a fuel alternative for a wide range of applications.[13–16] Among the most commonly used devices for water electrolysis, the current state-of-the-art MEA-architecture is the liquid-phase CEM-MEA, which consists of a solid-state CEM, catalyst layers, and transport media.[1] In a CEM-electrolyzer, the acidity of the CEM enforces acidic environments for both electrochemical half reactions in water electrolysis: the hydrogen-evolution reaction (HER) and oxygen-evolution

reaction (OER), which occur at the cathode and anode, respectively. In the acidic environment, the HER and OER proceed as follows,

$$4H^+ + 4e^- \rightarrow 2H_2, U^0 = +1.23 \text{ V vs. RHE} \quad (1)$$

$$2H_2O \rightarrow O_2 + 4H^+ + 4e^-, U^0 = 0 \text{ V vs. RHE} \quad (2)$$

It is often true that optimal conditions for the OER catalyst occur in a drastically different environment than that for the HER catalyst. For instance, most catalysts for the HER exhibit the lowest overpotentials in acidic environments.[17] Conversely, practically all low-overpotential, earth-abundant OER catalysts are only stable in alkaline environments.[17] Currently, CEM electrolyzers circumvent the stability issue by using expensive iridium or iridium oxide catalysts that can withstand acidic environments.[18] However, the use of precious-metal catalysts is cost prohibitive and undesirable, which motivates efforts to replace them with more affordable materials.[19] Therefore, the optimal configuration for a water electrolyzer would be one in which the cathode is at an acidic pH, while the anode is simultaneously maintained at an alkaline pH.

Similar behavior can be observed for other electrochemical processes. For instance, electrochemical CO_2 reduction[12] and ammonia synthesis[20] would benefit from use of a BPM under an applied pH gradient of pH 7 at the cathode and pH 14 at the anode. This differs slightly from the pH 0-14 gradient optimal for water electrolysis, with the pH 7 chosen at the cathode to depress HER selectivity. The benefits derived from operation under pH gradients even extend to the field of organic electrosynthesis; the cathodic organic electrosynthesis reaction of acrylonitrile to adiponitrile is most selective in near neutral pHs (~pH 7) due to solubility concerns of the organic reagents and selectivity concerns with HER[7,21] and would most desirably be paired with an oxygen evolving anode at pH 14. For methanol or ethanol oxidation, an applied pH gradient of pH 0-7 would be beneficial to pair efficient HER at the cathode with the near neutral environments of the

organic reagents at the anode.[22] Nonetheless, pH 7-7 operation is still relevant for solar-driven water splitting or seawater electrolysis applications.[4,23,24]

The pH gradients desired for water electrolysis and similar electrochemical reactions cannot be maintained in the uniformly acidic environment for a liquid-phase CEM-electrolyzer architecture. While the pH gradient could potentially be maintained by a constant flow of electrolyte on either side of the device, this is less practical because of the amount of electrolyte required. However, by substituting the CEM in the MEA with a bipolar membrane (BPM), which is composed of a cation-exchange layer (CEL) and an anion-exchange layer (AEL) laminated together, it becomes possible to maintain a pH gradient across the device and enable optimal conditions for the catalysis of both half reactions.[9,10,25–30]

A BPM is shown schematically in **Figure 1**. The CEL contains negative fixed-charge groups, such as sulfonate anions ($-SO_3^-$), that mitigate anion uptake in the CEL and enable the selective transport of cations.[31–33] Conversely, the AEL contains positive fixed-charge groups, such as quaternary ammonium cations ($-NH_4^+$), that enable selective transport of anions.[34,35] Both ion-exchange layers are typically 50 to 100 μm thick.[10,36,37] In some cases, a water dissociation catalyst layer (CL) is included at the junction between the AEL and CEL that is typically 2 to 10 nm thick and contains a weakly acidic or basic group that exhibits strong hydrogen-bonding to catalyze the dissociation of water into hydronium and hydroxide ions.[36,38] Recently, various metal oxides and graphene oxide have been explored as water-dissociation catalysts.[38–42]

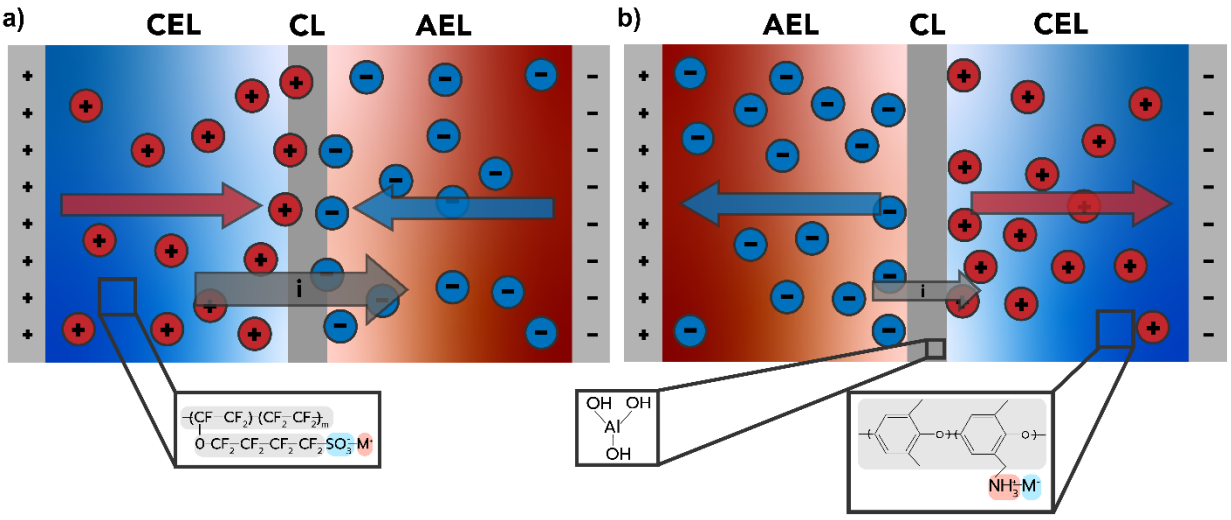

Figure 1: Schematic of a bipolar membrane with a cation-exchange layer, an anion-exchange layer and a catalyst layer in **(a)** forward and **(b)** reverse bias. As depicted in the insets, the CEL contains sulfonate negative fixed-charged groups, the AEL contains quaternary ammonium positive fixed-charge groups, and the water dissociation catalyst is $Al(OH)_3$. In the forward bias case, current (gray arrow) is driven by water recombination. For reverse bias, current is driven by water dissociation.

BPMs have two modes of operation as defined by the direction of the flow of current: reverse bias and forward bias.[43–45] In forward bias (**Figure 1a**), the CEL side of the BPM is held at high potential and the AEL side is held at low potential. Under this applied potential field, the cations in the CEL and the anions in the AEL will both move toward the AEL/CEL interface due to migration. For this operating mode, hydronium cations and hydroxide anions will recombine to form water at the interface, and high current densities can be achieved due to the rapid kinetics of recombination.[36,43,44]

In reverse bias (**Figure 1b**), the CEL is held at low potential and the AEL is held at high potential. In this case, the mobile charges in each ion-exchange layer will move away from the junction. This decreases the concentration of mobile ions in the catalyst layer, increasing the resistance of the BPM until a mass-transfer limited cross-over current is achieved.[36,46] Initially, the sluggish kinetics of water dissociation at the interface are insufficient to generate enough

hydronium and hydroxide ions.[44] However, as the applied potential difference in a reverse bias BPM increases, the BPM experiences a "breakdown", at which point the rate of water dissociation is sufficiently amplified by the electric field to overcome the rate of recombination, and consequently higher current densities are attained.[36,46,47] This phenomenon is known as the Second Wien Effect.[47] A water-dissociation catalyst is used to improve the kinetics of dissociation and minimize the applied potential required to achieve breakdown.[38,48] The reverse bias configuration is preferable for implementation in most electrolysis applications because it optimally pairs the positive potential at the anode with the AEL, enabling either alkaline or neutral oxidative chemistry, while simultaneously pairing the negative potential at the cathode with the CEL to enable acidic or neutral reductive chemistry.[10] Therefore, for the remainder of this work, the BPM will be considered in the reverse-bias configuration.

A number of experimental studies have utilized BPMs in reverse bias for water-electrolysis.[28,40,42,49–51] The electrochemical characteristics of these materials have been widely characterized using 4-probe experiments to deconvolute the membrane potential from the kinetic overpotentials at the working electrodes, effectively isolating the interfacial water dissociation.[10,29,41,46,50,52] Nonetheless, the phenomena controlling water dissociation in the interfacial catalyst layer are still poorly understood. Furthermore, while there have been some attempts to characterize the effects of ionic salt species, the influence of co- and counter-ion crossover during the operation of reverse bias BPMs continues to be a subject of discussion.[10,36] In particular, the effect of buffer reactions in the electrolyte remains unclear.[11]

In the study of BPMs, it is tempting to ignore ions other than hydronium (H_3O^+) or hydroxide (OH^-) present in the BPM and study only the dissociation of water into H_3O^+ and OH^-. However, the BPM can also uptake salt ions from the electrolyte and these species can transport

across the membrane. The salt ions are typically classified as either co-ions (salt ions in the electrolyte with the same charge as the adjacent ion-exchange layer) or counter-ions (salt ions in the electrolyte with opposite charge to the adjacent ion-exchange layer). Mitigating the transport of these co- and counter-ions is vital for developing stable BPM-electrolyzers because excess salt-ion crossover enables mixing of the electrolytes and results in the gradual neutralization of the applied pH gradient.[11] Crossover becomes even more relevant for CO_2 reduction, where the crossover of bicarbonate ions through the membrane would decrease CO_2 utilization at the cathode.[44] It is therefore necessary to describe the transport of the various species to find strategies to mitigate undesired salt ion crossover.

Modeling efforts for reverse bias BPMs attempted to replicate 4-probe experiments by solving the Poisson equation locally near the junction[47,53] or with continuum transport models of the entire BPM based on a modified Poisson-Nernst-Planck formulation that includes the Second Wien Effect.[36,37,48,54–57] Unfortunately, there is a dearth of studies that have attempted to simulate the electrochemical characteristics of BPMs under the high applied pH gradients relevant to implementation in water electrolyzers. Furthermore, the multicomponent nature of the multi-ion transport in the BPM under these conditions necessitates a more complex formalism that accounts for the myriad of interactions present.[32,58] Prior models also neglect water concentration gradients within the BPM, which are critical to driving ion transport within the BPM and can have significant effects on its mechanical properties.[31,41] Incorporating gradients in water content are thus necessary to assess the lifetime and performance of BPMs. Furthermore, while these models adequately capture the current/voltage characteristics measured experimentally at high current densities, where water dissociation dominates, they agree poorly in the low current-density regime, where

co- and counter-ion leakage is the main contributor to the ionic current.[36,37] This disagreement is indicative of an incomplete understanding of ion crossover.

In this paper, we present a comprehensive model that describes multi-ion transport and interactions, homogeneous reaction kinetics, and water-dissociation catalysis in a reverse-bias-operation BPM under various applied pH gradients and for electrolytes with varying buffer species. The model differs from those reported in prior studies in its treatment of homogeneous buffer kinetics and water uptake and is, to the best of our knowledge, the first to simulate the BPM under conditions relevant to efficient electrolysis and electrosynthesis. By capturing the effects of the aforementioned phenomena, the model is able to describe experimental polarization curves accurately for a Fumatech BPM in six distinct electrolyte environments.[10] The impact of electrolyte species, water uptake, membrane properties, and water-dissociation catalysts are examined in these various pH environments in order to inform future design of high-performance BPMs.

2. Computational Methods

This section describes the modeling approach, governing equations, and assumptions with the aim of providing the reader with an understanding of the methodology used to capture the complex physics of multi-ion transport in a reverse-bias BPM. The BPM model employed here is designed to mimic a 4-electrode experiment (**Figure 2a**), where an applied potential is measured between reference electrodes that probe electrostatic potential in close proximity to the two ends of the BPM through the use of Luggin capillaries.[10] By employing a 4-electrode experimental setup, the kinetic overpotentials associated with Faradaic reactions occurring at the working or counter

electrode are separated from the potential drop across the membrane, thereby allowing for isolated measurement of current/voltage characteristics of the BPM.

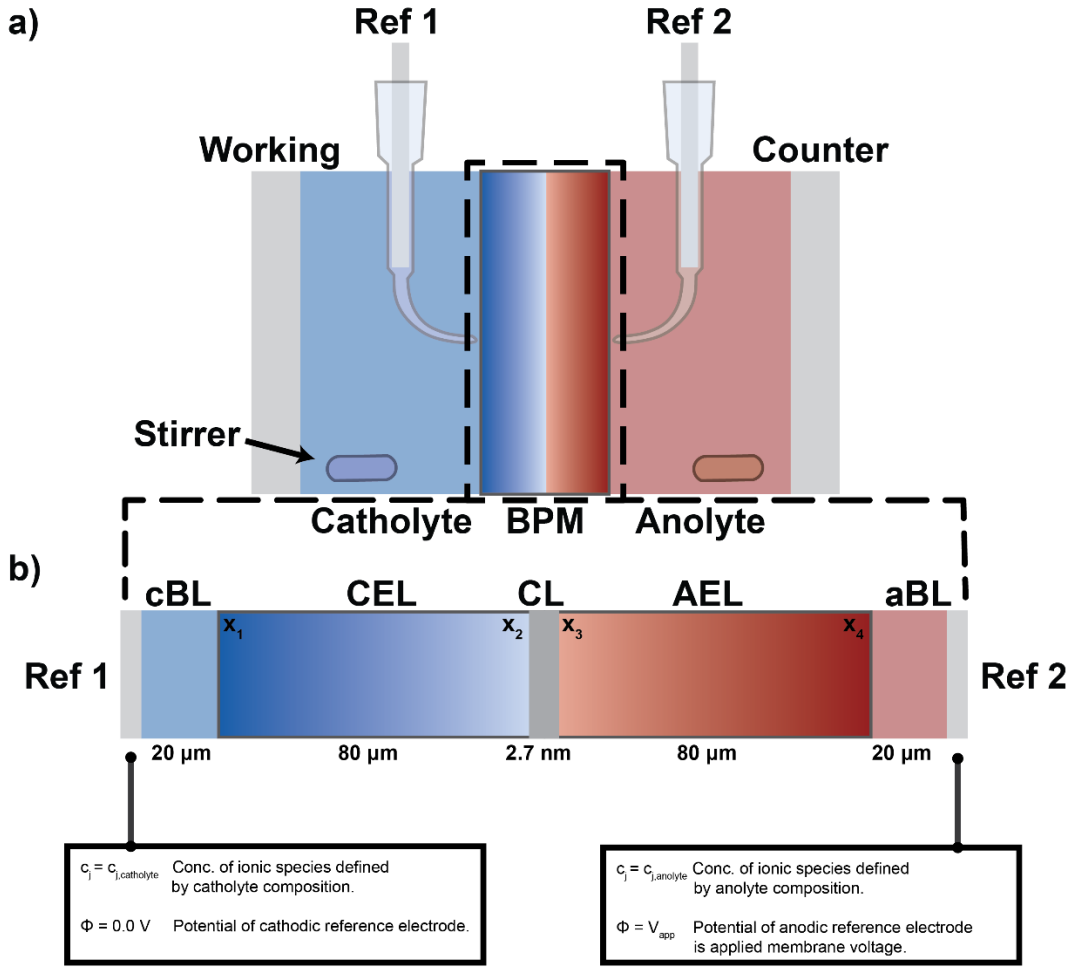

Figure 2: (a) A standard 4-probe experimental set up. **(b)** Schematic representation of model and boundary conditions.

The BPM is represented by a 1-dimensional model that consists of the region between and including the two reference electrodes in a 4-probe electrochemical cell. By modeling this domain, all physical phenomena relevant to the measured polarization curves are captured: the Donnan equilibrium between the electrolytes and the ion-exchange layers, the transport of ionic species within the ion-exchange layers, and the electric-field-enhanced water dissociation occurring at the AEL/CEL junction. As shown in (**Figure 2b**), the model comprises a cathodic reference electrode

(Ref 1), a 20 μm catholyte boundary layer (cBL), an 80 μm CEL, a 2.7 nm water-dissociation catalyst layer (CL), an 80 μm AEL, a 20 μm anolyte boundary layer (aBL), and an anodic reference electrode (Ref 2). The thickness of the ion-exchange layers is taken from manufacturer specifications (Fumatech) for the BPM used in the experiment.[10,59] The 2.7 nm thickness of the catalyst layer is a fitted parameter and is consistent with previous studies.[37] The thickness of the electrolyte boundary layers between the Luggin capillaries and the BPM were chosen for convenience, and the model results were insensitive to this choice (see Fig. S1.1 in the supporting information). All of the parameters characterizing the membrane and the two electrolytes are listed in **Table 1**. This table also lists the diffusion coefficients for all species, the dielectric coefficients of the membrane and water, and the rate and equilibrium constants for all reactions considered.

Table 1: List of model parameters and their source.

Parameter	Value	Unit	Ref.
Membrane			
L_{AEL}	80	μm	[59]
L_{CEL}	80	μm	[59]
IEC	1.81	mmol g^{-1}	[11]
$\rho_{M.wet}$	1.0	g mL^{-1}	[59]
L_{char}	0.58	nm	[36]
Electrolytes			
L_{aBL}	20	μm	Assumed
L_{cBL}	20	μm	Assumed
$c^0_{H_2O}$	55.56	mol L^{-1}	[60]

Aqueous Transport Properties			
$D_{K^+,w}$	1.96×10^{-9}	$m^2\ s^{-1}$	[61]
$D_{Na^+,w}$	1.33×10^{-9}	$m^2\ s^{-1}$	[61]
$D_{SO_4^{2-},w}$	1.07×10^{-9}	$m^2\ s^{-1}$	[61]
$D_{HSO_4^-,w}$	1.33×10^{-9}	$m^2\ s^{-1}$	[61]
$D_{HPO_4^{2-},w}$	6.9×10^{-10}	$m^2\ s^{-1}$	[61]
$D_{H_2PO_4^-,w}$	8.46×10^{-10}	$m^2\ s^{-1}$	[61]
$D_{H_3O^+,w}$	6.96×10^{-9}	$m^2\ s^{-1}$	[36]
$D_{OH^-,w}$	4.96×10^{-9}	$m^2\ s^{-1}$	[36]
ε_{H_2O}	6.934×10^{-10}	$F\ m^{-1}$	[36]
ε_M	1.96×10^{-11}	$F\ m^{-1}$	[36]
Homogenous Reactions			
K_1^0	3.26×10^{-18}		[36]
k_1^0	2.96×10^{-10}	$m^3\ (s\ mol)^{-1}$	[36]
k_{-1}^0	9.08×10^{7}	$m^3\ (s\ mol)^{-1}$	[36]
K_2	1.116×10^{-9}		[60]
k_2	0.1	$m^3\ (s\ mol)^{-1}$	Fit[1]
K_3	1.8×10^{-4}		[60]
k_3	10	$m^3\ (s\ mol)^{-1}$	Fit[1]

[1]Fitted forward rate constants were determined by increasing the order of magnitude of the rate constant until the respective phosphate and sulfate buffer species have achieved equilibrium throughout the modeled domain for all applied potentials.

2.1 Kinetics of Water Splitting

To understand the electrochemical characteristics of BPMs, careful attention must be given to the dissociation of water to hydroxide and hydronium ions that can occur throughout the domain,

$$2\mathrm{H_2O} \underset{k_{-1}}{\overset{k_1}{\rightleftharpoons}} \mathrm{H_3O^+} + \mathrm{OH^-} \tag{3}$$

Where k_1 and k_{-1} are the kinetic rate constants for water dissociation and recombination, respectively. For consistency with the kinetic parameters taken from Craig,[36] the bimolecular mechanism of water dissociation that involves the dissociation of two water molecules into hydroxide and hydronium is implemented as opposed to the pseudo-unimolecular dissociation mechanism of one water molecule splitting to proton and hydroxide. The bimolecular dissociation mechanism captures effects of changing water concentration between the membrane and electrolyte better. The equilibrium constant for this homogeneous reaction is tabulated with the electrochemical potentials measured against a molar ratio reference state (see Section S2 in the SI for the derivation) and is defined as

$$K_1^0 = \frac{k_1}{k_{-1}} = \frac{c_{OH^-} c_{H_3O^+}}{c_{H_2O}^2} \tag{4}$$

Prior studies have shown that the applied electric field at the junction of a BPM can achieve values up to 10^9 V m^{-1} attributed to the rapid change in background charge of the BPM at the AEL/CEL interface.[46,47] Under these very high fields, it is proposed that the rate of water dissociation is enhanced significantly, a phenomenon known as the Second Wien Effect, while the recombination rate changes only slightly, pushing the equilibrium towards dissociation.[36,62] To describe this phenomenon physically, first consider an undissociated water molecule as a dipole

capable of dissociating. Thermodynamically, when an electric field E is applied, the Gibb's Free Energy of the Bjerrum dipole is reduced,[37,63]

$$\Delta G(E) - \Delta G(0) = -l_B eE, \qquad l_B = \frac{e^2}{4\pi\varepsilon k_B T} \tag{5}$$

where e is the elementary charge, l_B is the Bjerrum length, ε is the permittivity of free space, k_B is Boltzmann's constant, and T is the absolute temperature. This reduction in Gibb's Free Energy results in a corresponding increase in the generation rate of ions, and thus the dissociation rate,[62]

$$\frac{k_1(E)}{k_1^0} = \exp\left(\frac{l_b eE}{k_B T}\right) = \exp\left(\frac{l_b FE}{RT}\right), \tag{6}$$

where k_1^0 is the dissociation rate coefficient in the absence of an applied electric field, F is Faraday's constant, and R is the ideal-gas constant. The value for k_1^0 is determined from the rate coefficients determined by Craig[36] evaluated at a temperature of 298 K. In prior studies,[46,47,53] this un-catalyzed electric-field dependence has been represented in the form

$$\frac{k_1(E)}{k_1^0} = \exp(\beta E), \tag{7}$$

where $\beta = \frac{l_b F}{RT}$ as per comparison with Eq. (6). We note that the form of Eq. (7) is consistent with the Butler-Volmer equation for describing the electrochemical kinetics of Faradaic charge-transfer reactions at solid electrodes.[64] More complicated kinetic models have been proposed for the dissociation kinetics of water-dissociation on various catalysts.[36,37] However, for simplicity in considering the impact of the catalyst, and due to the uncharacterized nature of water-dissociation catalysis for the Fumatech BPM, we choose to adopt an exponential behavior for the Second Wien Effect.

To incorporate the effect of the water-dissociation catalyst layer into the treatment of the Second Wien Effect, similarity in behavior to Butler-Volmer kinetics is invoked and a parameter

α, which will be referred to as the catalyst effectiveness factor, is introduced that is treated like the charge-transfer coefficient in the Butler-Volmer equation,

$$\frac{k_1(E)}{k_1^0} = \exp(\alpha\beta E) \tag{8}$$

where α is defined to be 1 in all regions outside of the water-dissociation catalyst layer, preserving the proposed kinetics of the non-catalytically assisted water dissociation (Eq. 7). On the other hand, in the 2.7 nm thick catalyst layer, the value of α is fit to a value of 1.8. Because there is no explicit treatment of both an un-catalyzed and a catalyzed pathway within the catalyst layer, this effectiveness factor should be thought of as describing a composite of both pathways.

Recombination is also impacted by the presence of an applied electric field, albeit to a much lesser extent. By following the methodology of Onsager and Fuoss,[65] one can derive the following formulation for the recombination rate constant:[36]

$$\frac{k_{-1}(E)}{k_{-1}^0} = 1 + \frac{1 - \exp\left(-\frac{1}{\sigma}\right)}{2}\left(\sigma^2\beta\mathrm{E} + (4.97\sigma)\frac{\sinh(0.0835\sigma\beta\mathrm{E})}{\cosh^2(0.0835\sigma\beta\mathrm{E})}\right), \sigma = \frac{a}{2l_B} \tag{9}$$

The parameter σ represents a dimensionless bond length for recombination and is based on the physical bond length for water dissociation and recombination where a = 0.58 nm.[36]

2.2 Homogeneous Buffer Reactions

In addition to the dissociation of bulk water within the BPM, the homogeneous buffer reactions of the co- and counter-ions are considered. Doing so contributes to a complete electrochemical description of the BPM, which is critical at low current densities where co- and counter-ion transport dominate. For the electrolytes studied (i.e., sulfate and phosphate), these buffer reactions, which occur in both the aqueous and ionomer phases, are given by

$$H_2PO_4^- + H_2O \underset{k_{-2}}{\overset{k_2}{\rightleftharpoons}} H_3O^+ + HPO_4^{2-} \tag{10}$$

$$HSO_4^- + H_2O \underset{k_{-3}}{\overset{k_3}{\rightleftharpoons}} H_3O^+ + SO_4^{2-} \tag{11}$$

Both buffer reactions are considered in their bimolecular form for consistency with the bimolecular water dissociation mechanism employed in the present study (see Eq 3). The equilibrium constants, K_i, for reactions (10) and (11) are taken from literature[60] and converted to the molar ratio reference (see derivation in Section S2 of SI) with the values given in **Table 1**. In this model, the first buffer dissociation is assumed to be complete and the molecular forms of sulfuric acid or phosphoric acid are assumed to be absent. Additionally, while hydrogen phosphate (HPO_4^{2-}) can further dissociate to phosphate (PO_4^{3-}) anions, because the K_a for hydrogen phosphate is very small (K_a= 4.2 x 10^{-13}), this dissociation is neglected.

The forward rate coefficients for all dissociation reactions are taken to be large enough to ensure equilibrium of the buffered species throughout the domain over the range of applied membrane potential (0 to 1 V). The rate coefficients for the reverse reactions are given by

$$K_n = \frac{k_n}{k_{-n}} \tag{12}$$

Work by Divekar *et al.* suggests that the rate coefficients and the unimolecular K_a of the buffer reactions change when measured in an ionomer environment as opposed to an aqueous solution.[66] Because the magnitudes of these differences have yet been established, and likely vary with membrane hydration, co- and counter-ion identity, etc., they are neglected in this study.[67–69]

2.3 Treatment of Membrane Fixed-Charge

The fixed-charge density between the different regions in the membrane is modeled using hyperbolic tangents,[36]

$$c_M(x) = \frac{\rho_{M,dry} \times IEC}{2}\left(\tanh\left(\frac{x - x_3}{L_{char}}\right) - \tanh\left(\frac{x - x_4}{L_{char}}\right) + \tanh\left(\frac{x - x_2}{L_{char}}\right) - \tanh\left(\frac{x - x_1}{L_{char}}\right)\right), \quad (13)$$

Here, x is the position as measured from the center of the BPM. x_1 is the leftmost point of the CEL, x_2 is the leftmost point of the catalyst layer, x_3 is the leftmost point of the AEL, and x_4 is the leftmost point of the anolyte boundary layer (see **Figure 2: (a)** A standard 4-probe experimental set up. **(b)** Schematic representation of model and boundary conditions.). This distribution is illustrated in Fig. S3. Eqn. 13 allows for smooth, differentiable transitions (*i.e.*, a smoothed step function) at the interface between the electrolyte and ionomer phases as well as between the AEL and CEL. The hyperbolic tangents in this study have a characteristic length of L_{char} = 0.58 nm, which is the characteristic bond length for water dissociation derived by Craig, and represents the length at which the hydroxide and hydronium ions separate and start to diffuse apart from one another.[36]

2.4 Electrochemical Potentials

To construct a thermodynamically consistent model, expressions for the electrochemical potential of the various ionic species are required.[64] For the BPM, these electrochemical potentials are dependent on temperature, pressure, composition, electrostatic potential, and applied electric field.[36] For the present study, the system is assumed isothermal at 298 K and isobaric at 1 bar pressure. The electrochemical potentials employed (see **Table 2**) are also defined based on the molar ratio of the ionic species concentration to the local water concentration to capture membrane hydration effects on electrochemical potential.[36] Because the electrochemical potential is solved

for in all aqueous and ionomer phases and for all ionic species, Donnan equilibrium with the bulk electrolyte is implicitly obeyed in terms of the partitioning of the ionic species between the ionomer phase and the bulk electrolyte (see Section S4 for Donnan equilibrium calculation).[6]

Table 2: Chemical and electrochemical potentials of species present in model. $\mu^0_{H_2O}$ is the chemical potential of pure water at 1 bar. For any ionic species, $\tilde{\mu}_i^0$ is a reference state for species *i* in water at 1 bar, c_i is the concentration of species *i*, c_i^0 is the concentration of the species *i* at the reference conditions, z_i is the charge of the ion, and Φ is the macroscopic electrostatic potential.

Species	Potential	
H_3O^+	$\tilde{\mu}_{H_3O^+} = \tilde{\mu}^0_{H_3O^+} + RT\ln\left(\frac{c_{H_3O^+}c^0_{H_2O}}{c^0_{H_3O^+}c_{H_2O}}\right) + F\Phi + RT\ln\left(\gamma^E_{\pm}\right)$	(14)
OH^-	$\tilde{\mu}_{OH^-} = \tilde{\mu}^0_{OH^-} + RT\ln\left(\frac{c_{OH^-}c^0_{H_2O}}{c^0_{OH^-}c_{H_2O}}\right) - F\Phi + RT\ln\left(\gamma^E_{\pm}\right)$	(15)
Co- and Counter-ions	$\tilde{\mu}_i = \tilde{\mu}^0_i + RT\ln\left(\frac{c_i c^0_{H_2O}}{c^0_i c_{H_2O}}\right) + z_i F\Phi$	(16)

For the special case of hydronium and hydroxide, an electric-field-dependent activity coefficient, $\gamma^E_{\pm}$, is needed to maintain thermodynamic consistency due to the electric-field dependence of the dissociation equilibrium resulting from the Second Wien Effect. This field-dependent activity coefficient is determined by solving for the activity coefficient necessary to satisfy equilibrium between the hydronium, hydroxide, and water ($\tilde{\mu}_{H_3O^+} + \tilde{\mu}_{OH^-} = 2\mu_{H_2O}$) throughout the domain.

$$\gamma^E_{\pm} = \sqrt{\frac{k^0_1 k_{-1}(E)}{k^0_{-1} k_1(E)}} \tag{17}$$

2.5 Transport Equations

The fluxes of the mobile ions are governed by the generalized Nernst-Planck equation,

$$N_i = -\frac{D_i c_i}{RT}\frac{d\tilde{\mu}_i}{dx}, \tag{18}$$

where N_i is the molar flux of species *i,* and D_i is the diffusivity of species *i*. Nernst-Einstein relationship is used to relate mobilities and diffusivities. Substitution of Eqs. 14-16 into Eq. 18 yields the flux of each individual ionic species, as shown in **Table 3**.

Table 3: Flux of ionic species in model.

Species	**Flux**	
H_3O^+	$N_{H_3O^+} = -D_{H_3O^+}\frac{dc_{H_3O^+}}{dx} + D_{H_3O^+}c_{H_3O^+}\frac{d\left(\ln\left(c_{H_2O}\right)\right)}{dx} + D_{H_3O^+}c_{H_3O^+}\frac{FE}{RT} - D_{H_3O^+}c_{H_3O^+}\frac{d\left(\ln\left(\gamma_{\pm}^{E}\right)\right)}{dx}$	(19)
OH^-	$N_{OH^-} = -D_{OH^-}\frac{dc_{OH^-}}{dx} + D_{OH^-}c_{OH^-}\frac{d\left(\ln\left(c_{H_2O}\right)\right)}{dx} - D_{OH^-}c_{OH^-}\frac{FE}{RT} - D_{OH^-}c_{OH^-}\frac{d\left(\ln\left(\gamma_{\pm}^{E}\right)\right)}{dx}$	(20)
Co- and Counter-ions	$N_i = -D_i\frac{dc_i}{dx} + D_i c_i\frac{d\left(\ln\left(c_{H_2O}\right)\right)}{dx} + z_i D_i c_i\frac{FE}{RT}$	(21)

Typically, Stefan-Maxwell diffusion is used to capture species/species interactions that are significant in concentrated systems. Unfortunately, because our model describes the transport of up to seven ionic species, implementation of the Stefan-Maxwell framework would require an additional 42 degrees of freedom as well as the determination of composition-dependent diffusion coefficients for the frictional interactions between the seven salt ion species, water, and the membrane. This would increase the uncertainty and complexity of the numerical model considerably; consequently, the Nernst-Planck equation is used even though the conditions are not necessarily dilute. We also note that in the present study, we only simulate current densities up to 10 mA cm^{-2}, for which dilute-solution theory has been found to be sufficiently accurate.[70]

The diffusion coefficients for a given ionic species, D_i, depend upon the phase. In the aqueous electrolyte phases, these diffusion coefficients are equal to their values in pure water, $D_{i,w}$. In the ionomer phase, the effective diffusion coefficients for each ionic species, $D_{i,eff}$ are calculated following work of Grew *et al.*[6,71,72]

$$D_{i,eff} = \frac{\phi_L^q D_{i,w}}{x_w(1+\frac{1}{\lambda}\zeta_i)} \tag{22}$$

In this framework, q is a fitting parameter related to the tortuosity of the ionomer and x_w is the ratio of the moles of water in membrane to the sum of the moles of water and fixed-charge groups given by

$$x_w = \frac{\lambda}{1+\lambda} \tag{23}$$

where λ is the hydration of the ion-exchange layer defined as the ratio of water molecules in the ionomer to fixed charge groups. ϕ_L is the water volume fraction in the ionomer,

$$\phi_L = \frac{\lambda V_w}{\lambda V_w + V_M} \tag{24}$$

where V_w and V_M are the molar volumes of pure water and membrane, respectively. The parameter ζ_i describes the ratio of the species-water and species-membrane diffusivities and can be approximated by kinetic theory,[73]

$$\zeta_i = \frac{D_{i,w}}{D_{i,M}} = \left(\frac{V_M}{V_w}\right)^{\frac{2}{3}} \left(\frac{M_{i,M}}{M_{i,w}}\right)^{\frac{1}{2}} \tag{25}$$

where $M_{i,M} = (\frac{1}{M_i} + \frac{1}{M_M})$ is the reduced molar mass.

From these fluxes, material balances for each species provide governing equations for the steady-state model,

$$\frac{dN_i}{dx} = R_i \tag{26}$$

where R_i is the production of species i from homogeneous chemical reactions,

$$R_i = \sum_n s_{i,n}\left(k_n \prod_{s_{i,n}<0} c_i^{-s_{i,n}} - k_{-n} \prod_{s_{i,n}>0} c_i^{s_{i,n}}\right) \tag{27}$$

where $s_{i,n}$ is the stoichiometric coefficient of species i in reaction n.

To solve for the potential, Poisson's equation is employed

$$-\frac{d^2\Phi}{dx^2} = \frac{F}{\varepsilon}\left(c_M(x) + \sum_i z_i c_i\right), \tag{28}$$

where ε is the permittivity of the medium and is expected to vary from the aqueous solution to the membrane. The permittivity of the BPM is expected to be similar to that of a dioxane-water mixture and is given as a function of the local water content by Craig,[36,74,75]

$$\varepsilon = \left(\frac{c^M_{H_2O}}{c^0_{H_2O}}\varepsilon^{-1}_{H_2O} + \varepsilon_M^{-1}\left(1 - \frac{c^M_{H_2O}}{c^0_{H_2O}}\right) + \varepsilon_3^{-1}\right)^{-1}, \tag{29}$$

where ε_M is the permittivity of the pure dioxane, ε_{H_2O} is the permittivity of pure water, and ε_3 is a mixing term that takes into account interactions between the ionomer and absorbed water.

$$\varepsilon_3 = \varepsilon_0\left(\frac{-2.42\left(1-\frac{c^M_{H_2O}}{c^0_{H_2O}}\right)\frac{c^M_{H_2O}}{c^0_{H_2O}}}{-0.48\left(1-\frac{c^M_{H_2O}}{c^0_{H_2O}}\right)-5.03\frac{c^M_{H_2O}}{c^0_{H_2O}}} + 0.066\left(1-\frac{c^M_{H_2O}}{c^0_{H_2O}}\right)\frac{c^M_{H_2O}}{c^0_{H_2O}}\right)^{-1} \tag{30}$$

This mixing term is quite significant and can account for up to a 40 % difference in permittivity for a BPM fully exchanged with hydronium or hydroxide.

Lastly, the electric field and electrostatic potential are related by

$$\frac{d\Phi}{dx} \equiv -E \tag{31}$$

2.6 BPM Water Uptake

It has been shown that the water uptake in BPMs is significantly lower from that in Nafion or other well-characterized ionomers ($\lambda = 9$ for a BPM vs. $\lambda = 21$ for Nafion).[11,76,77] There is a lack of available data regarding the transport coefficients or water-uptake isotherms for BPMs, and measured properties of monopolar membranes is not a sufficient proxy for modeling BPM water transport. Therefore, rather than solving for the water chemical potential and water flux explicitly, which are nontrivial and quite complicated. the concentration of water in the BPM is assumed to follow a complementary functional form to that for the fixed charge (Eq. 13). Therefore, the water concentration is given by

$$c_{H_2O}(x) = \frac{c^0_{H_2O}}{2}\left(2 - \tanh\left(\frac{x - x_1}{L_{char}}\right) + \tanh\left(\frac{x - x_4}{L_{char}}\right)\right) + \frac{c^M_{H_2O}}{2}\left(\tanh\left(\frac{x - x_1}{L_{char}}\right) - \tanh\left(\frac{x - x_4}{L_{char}}\right)\right), \tag{32}$$

where $c^0_{H_2O}$ is the concentration of pure aqueous phase water (55.56 M), and $c^M_{H_2O}$ is the concentration of water in the ionomer phase,

$$c^M_{H_2O} = \lambda(\rho_{M,wet} \times IEC) \tag{33}$$

where $\rho_{M,wet}$ is the density of the hydrated membrane and *IEC* is the ion-exchange capacity of the BPM. These parameters are assumed to be the same for both layers.

The water content, λ, defined as the molar ratio of water to fixed ion-exchange group, in the CEL and AEL are dependent on the internal hydronium or hydroxide content (see Fig. S5),[32]

$$\lambda_{\mathrm{CEL}} = \lambda_{f_{\mathrm{H_3O^+}=0}} + f_{\mathrm{H_3O^+}}\lambda_{f_{\mathrm{H_3O^+}=1}} \quad (34)$$

$$\lambda_{AEL} = \lambda_{f_{OH^-=0}} + f_{OH^-}\lambda_{f_{OH^-=1}} \quad (35)$$

where $\lambda_{f_{H_3O^+=0}}$ and $\lambda_{f_{OH^-=0}}$ are the hydration of a completely salt ion-exchanged CEL and AEL, respectively, $\lambda_{f_{H_3O^+=1}}$ is the hydration of the proton-form CEL, and $\lambda_{f_{OH^-=1}}$is the hydration of the hydroxide-form AEL. $f_{H_3O^+}$ is the fraction of hydronium ions calculated at every point in the CEL,

$$f_{H_3O^+} = \frac{c_{H_3O^+}}{IEC \times \rho_{M,wet}} \quad (36)$$

f_{OH^-} is the fraction of hydroxide ions calculated at every point in the AEL,

$$f_{OH^-} = \frac{c_{OH^-}}{IEC \times \rho_{M,wet}} \quad (37)$$

$\lambda_{f_{H_3O^+=0}}$ and $\lambda_{f_{OH^-=0}}$ are both fit to a value of 6 in order to ensure consistency between the salt-ion current in the measured and simulated polarization curves, and are consistent with lower uptake of salt forms of the membranes.[31,32,76] $\lambda_{f_{H_3O^+=1}}$ and $\lambda_{f_{OH^-=1}}$ are both taken from measurements of BPM water uptake in DI water (λ = 9).[11]

As noted in the previous subsections, explicit water species/membrane interactions are not included in the model. However, such interactions are included implicitly in the treatment of water uptake, diffusivity, and dielectric permittivity. These interactions will be important to model but are beyond the scope of the current study, largely because these interactions in BPMs have not yet been characterized fully and will likely differ substantially from those measured in monopolar membranes. Further experimental work is necessary to characterize BPM transport properties so that they can be implemented in future transport studies.

2.7 Boundary Conditions

The boundary conditions for the model are comprised of Dirichlet boundary conditions at each reference electrode. The potential of Ref 1 is held at 0.0 V, and the potential of Ref 2 is set to the applied membrane potential as measured experimentally. The concentration of the ionic species at Ref 1 (the catholyte boundary) is the concentration of the ionic species present in the bulk catholyte. Similarly, the concentration of the ionic species at Ref 2 (the anolyte boundary) is the concentration of ionic species in the bulk anolyte. Four pH environments are considered that are relevant to efficient electrolysis and electrosynthesis, as previously discussed, and correspond to those of Vermaas *et al.*[10]: a neutral pH 7-7 environment with both catholyte and anolyte as a mixture of 0.45 M K_2HPO_4 and 0.55 M KH_2PO_4 (this will be referred to as 1 M $K_iH_jPO_4$ where i + j = 3); a pH 0-7 environment with a 1 M H_2SO_4 catholyte and a 1 M $K_iH_jPO_4$ anolyte, a pH 7-14 environment with a 1 M $K_iH_jPO_4$ catholyte and a 1 M KOH anolyte, and a 0-14 pH environment with a 1 M H_2SO_4 catholyte and a 1 M KOH anolyte. In addition to the electrolyte pairs considered by Vermaas *et al.*,[10] polarization curves were collected experimentally (see Section S6 in the SI for experimental protocol) and modeled for a pH 0-7 environment with a 1 M HCl catholyte and either a 1 M Na_2SO_4 or 1 M $K_iH_jPO_4$ anolyte.

2.8 Numerical Methods

The governing equations (ionic species material balances and Poisson equation) were modeled in the General Form PDE Module and were solved with the MUMPS general solver in COMSOL Multiphysics 5.5 with a relative tolerance of 0.001. (See equations presented in Section S7) The modeling domain was discretized with a nonuniform mesh comprised of 1084 elements, which used an exponential refinement near the electrolyte/ionomer and AEL/CEL interfaces in order to

capture the sharp concentration gradients of about 0.58 nm characteristic length. A mesh independence study was performed (see Fig. S1.2 in the supporting information), revealing that a mesh of at least 412 domain elements is required to achieve convergence. For meshes finer than 412 elements, the model is completely independent of the chosen domain meshing.

3. Results and Discussion

3.1 Polarization curves for various electrolytes

Simulations were conducted for the four electrolyte environments investigated experimentally by Vermaas *et al.*[10] For each of the four environments, the model was fit to the measure polarization curve by adjusting the fitting parameters listed in Table S8. These fitting parameters are the same for all four pH environments. As seen in **Figure 3**, the model exhibits the characteristics of typical BPM polarization curves. There is an initial regime between 0.0 and ~0.6 V that is strongly mass-transfer limited and corresponds to the crossover of electrolyte salt ions. Beyond ~0.6 V, the electric field at the junction becomes sufficient to shift the equilibrium for water dissociation towards dissociation through the Second Wien Effect, and the BPM enters a water-dissociation-controlled regime, where the current is primarily dictated by the production of hydronium and hydroxide ions at the interface.[29,36] These distinct regimes are well represented in the polarization curves for pH 7-7, pH 0-7, and pH 7-14. The pH 0-14 case does not exhibit a salt-ion transport regime because the large dissociation and recombination currents present in this pH environment obscure the co- and counter-ion crossover. In contrast to earlier models, which have had difficulty capturing electrochemical characteristics of the BPM in the salt ion-leakage regime, the agreement between the model and experimental results is quite strong throughout the entire window of applied potentials. This model is also one of the first to capture the effects of an applied pH

gradient. This is an important advance because it provides critical insights needed for the implementation of BPMs in electrolyzers with optimal environments for HER and OER.[10,11,25]

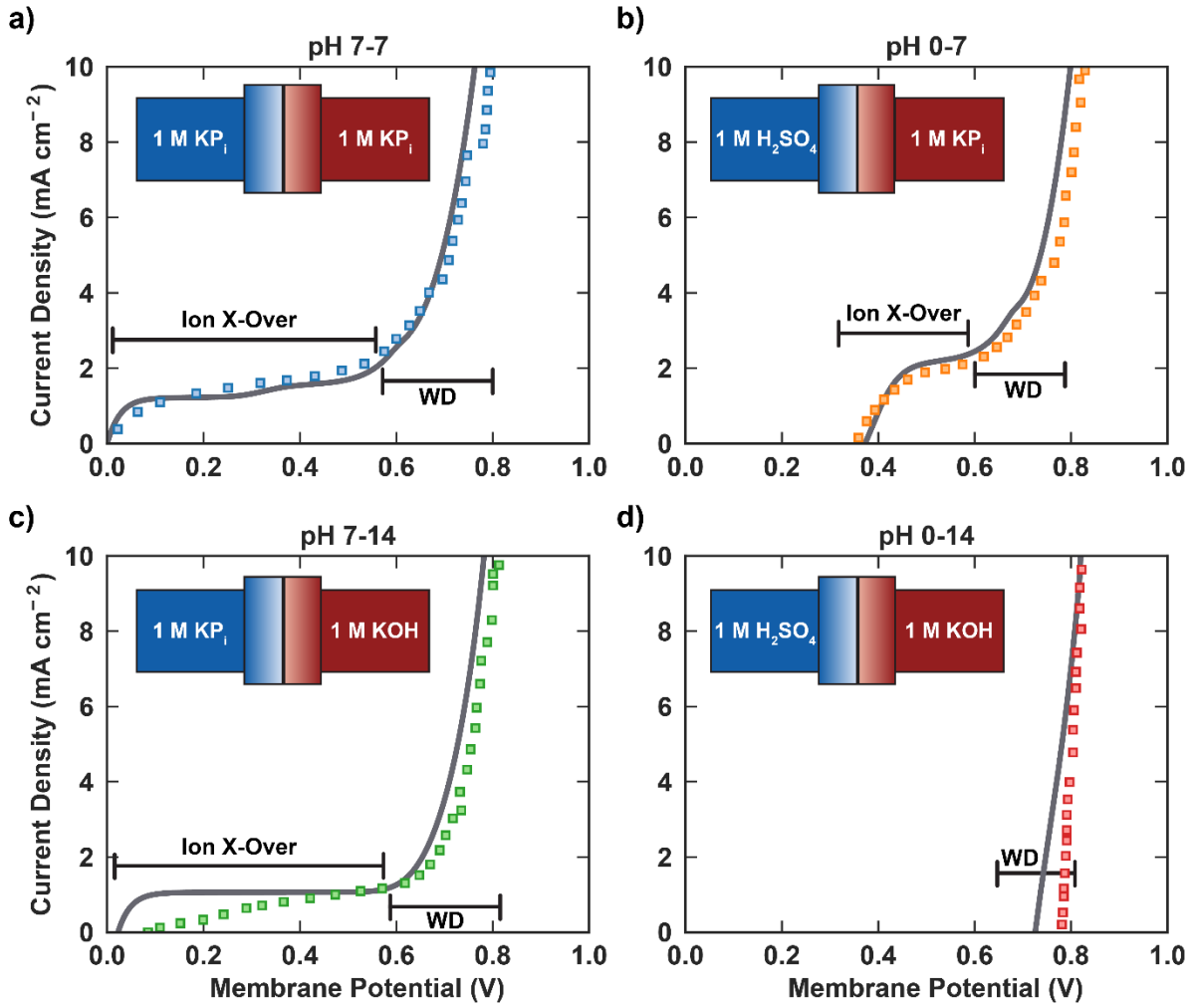

Figure 3: Calculated (solid lines) and measured (markers) polarization curves describing electrochemical behavior of bipolar membranes across various pH gradients. Experimental curves measured by Vermaas.[10] Brackets depict the regimes (salt-ion crossover and water dissociation) present in each polarization curve. Inset schematic displays corresponding electrolyte combination for each modeled polarization curve.

Although the simulated polarization curves agree very well with those observed experimentally within the water dissociation regime for all pH ranges explored, there is some disagreement between the simulated and experimental polarization curves for the salt-ion crossover regime for pH 7-7 and pH 7-14. Specifically, while the mass-transfer limit (~1 mA cm-

^{2}) is identical for both the modeled and experimental polarization curves for pH 7-14, the experimental curve attains its mass-transfer limit at a much higher membrane potential, whereas the simulated polarization curve has a much sharper and earlier transition to the mass-transfer limited regime. Additionally, while the simulated curve for pH 7-7 exhibits two distinct plateaus in current density, the experimental data from Vermaas does not. These discrepancies can be initially rationalized by recognizing that the simulations presented here assume a steady-state, whereas the experiments reported by Vermaa *et al.* were carried out using a galvanostatic sweep of 0.03 mA cm^{-2} s^{-1}.[10] Because of the transient nature of the galvanostatic sweep, it is possible that during the experiments the BPM did not have ample time to achieve equilibrium in the salt-ion regime, and consequently a slower approach to its mass-transfer limitations for pH 7-14 was observed. This slower approach to equilibrium also obscures the distinct plateaus for the 7-7 case. Nonetheless, we find the steady-state model adequately captures the essential physics of the BPM in these environments; modeling a transient BPM is beyond the scope of the current work.

3.2 Analysis of Partial Current Densities in a BPM

In addition to describing the polarization curve for a BPM, the model can be used to decompose the current density into the partial-current-density contributions for each ionic species. The ability to do so is important because there is still disagreement between experimentalists regarding the primary carrier of current in each regime of the polarization curve. Most investigators have argued that in the mass-transfer-limited regime, referred to above as the salt-ion crossover regime, the current is solely due to the transport of electrolyte salt ions.[29,38] However, by fully modeling and deconvoluting the contributions of individual ions to current density in the pH environments explored, the present model demonstrates that while the plateau current density is largely

dominated by the transport of salt ions, hydronium, and hydroxide ion currents generated by water dissociation account for a significant portion of the overall current density.

Figure 4 displays the polarization curves (grey curves) decomposed into their contributions (colored curves) for each ionic species for the four pH environments modeled. Due to different background charges in each ionomer layer, there are stark differences in the ionic currents in each layer. The current in the CEL is primarily carried by cations, and the current in the AEL is carried by anions. Therefore, the partial current densities for the CEL (**Figure 4a-d**) and AEL (**Figure 4e-h**) are distinct from one another. In examining these partial-current distributions, the argument for a distinct salt-ion crossover regime and a distinct water-dissociation regime becomes clear. As shown in Fig. 4e-g, at low current densities, the current density in the CEL is dominated initially by potassium transport (orange curves). However, once significant water dissociation occurs (referred to as breakdown) and hydronium cations are generated in the CEL, the shape of the polarization curve becomes dictated by the hydronium partial current density (red curves). This conclusion is further demonstrated in the partial current distributions in the AEL (**Figure 4e-h**). For low current densities, potassium and phosphate-species (green curves) crossover dominate the electrochemical behavior. However, when breakdown is achieved at high current densities, a sharp transition is visible into a regime where hydroxide ions formed at the interface account for most of the current carried in the AEL. This demonstrates that the plateau observed in the polarization curve is indeed due to mass-transfer-limited co- and counter-ion crossover.

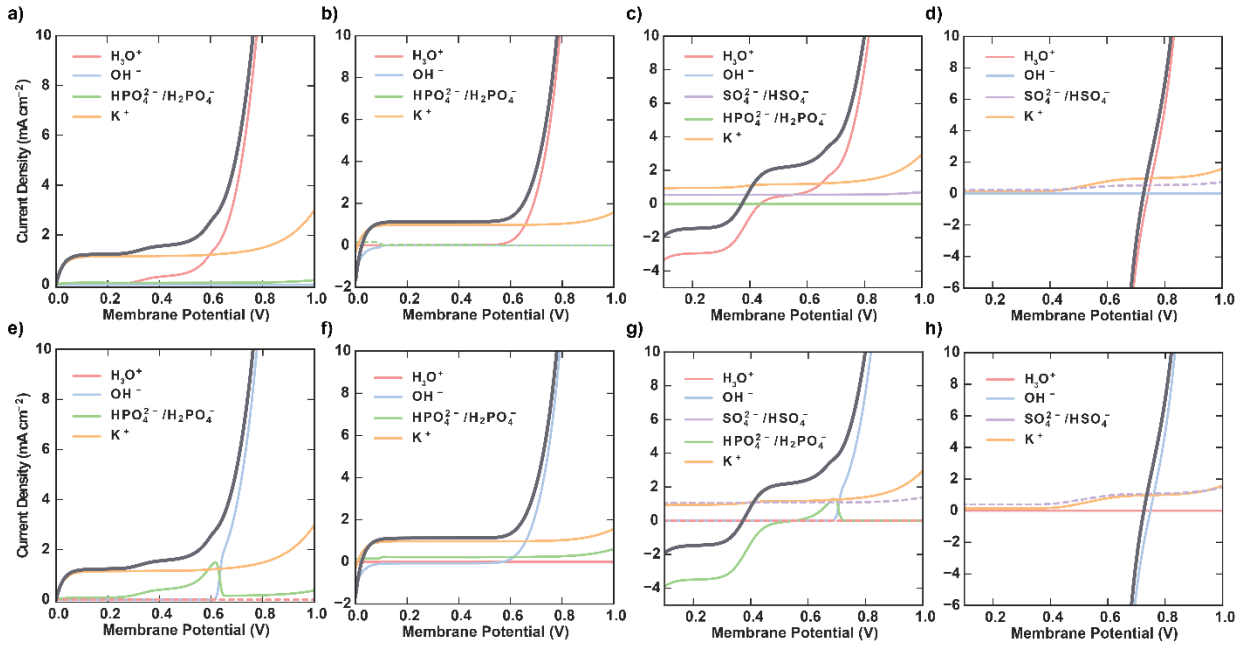

Figure 4: Analysis of partial current densities in the BPM. **(a-d)** Polarization curve breakdown into partial current density contributions for species in the CEL. **(e-h)** Polarization curve breakdown into partial current density contributions for species in the AEL. Dashed lines are purely for visibility of overlapping lines.

These two distinct regimes are not observed for the case of pH 0-14. As shown in **Figure 4d** and **Figure 4h**, the current is carried by the electrolyte salt ions. The potassium (orange) and sulfate (purple) currents achieve a value of up to ~1.5 mA cm^{-2} for a membrane potential of 1 V, which is comparable to the co- and counter-ion current achieved in other pH environments. Hence, the salt-ion contributions thus account for a significant portion of the overall current. However, the salt-ion contribution is almost totally obscured due to the steep slopes of the hydronium and hydroxide currents carried in the CEL and AEL, respectively.

To address the distribution of ionic current densities in the plateau current density, the fractions of the total current carried by hydronium and hydroxide ions were calculated (partial current divided by total current) and plotted against total current density (Fig. S9). As seen in Fig. 4, the plateau in current densities for the polarization curves occur at ~1 to 2 mA cm^{-2}. Calculation

of the fraction of the current due to water dissociation at these current densities (Fig. S9) reveals that water dissociation is responsible for up to 40 % of the current in the plateau. This demonstrates that while co- and counter-ion crossover does indeed dominate at low current densities and applied potentials, interfacial water dissociation is responsible for a non-negligible portion of the measured current.

3.3 Hydronium and Hydroxide Concentration Polarization and Transport Mechanisms

Concentration gradients in hydronium and hydroxide ions are particularly relevant when considering a BPM device, where the gradients affect membrane water uptake and drive ionic transport.[32,77] Vermaas *et al.* hypothesized that hydronium and hydroxide concentration polarization would occur within the BPM due to the generation of ions from water dissociation at the CEL/AEL interface.[10] Additionally, Sun *et al.* hypothesized that the concentration polarization would be greater within the AEL than in the CEL due to the lower diffusivity of hydroxide in comparison to hydronium.[28] Both of these effects are captured well by the model for ion-exchange layers in contact with a neutral electrolyte (**Figure 5a**). At potentials larger than the breakdown potential, strong concentration gradients in the simulated hydronium and hydroxide profiles form to preserve electroneutrality with the salt ions within the BPM. These concentration gradients are generated as follows. At the AEL/CEL interface, both hydronium and hydroxide species achieve maximum concentrations due to water dissociation. Conversely, at the ionomer/electrolyte interfaces, the hydronium and hydroxide concentrations are significantly lower consistent with the Donnan equilibrium between the ionomer and the neutral electrolyte phases. Moreover, the simulated hydroxide concentration gradients at a given voltage are larger than the corresponding hydronium gradients. As the applied voltage increases, the degree of concentration polarization observed also increases, which corresponds to an increase in ion transport by diffusion.

In contrast to the hypothesis of Vermaas *et al.*[10], concentration polarization is not apparent for a CEL in contact with a highly acidic (pH 0) or an AEL in contact with a highly alkaline (pH 14) electrolyte. For these cases, because the hydronium or hydroxide ions are the majority carriers in the electrolyte solution, the corresponding ion-exchange layer is already fully exchanged with hydronium or hydroxide once Donnan equilibrium is achieved. The dissociation of water at the interface is therefore incapable of imposing concentration gradients in the hydronium and hydroxide ions the membrane, and the gradients in electrostatic potential (Fig. S10) must be the driving force for the migration of hydronium and hydroxide. Prior work in BPMs has consistently reinforced the concept that all gradients in electrostatic potential outside of the bipolar junction are negligible.[28,46,47] While these electrostatic potential gradients in the bulk ionomer are small (as depicted in Fig. S10), the current study finds that for an ion-exchange layer in contact with a strong acid or base, migration is indeed the dominant mode of transport for hydronium or hydroxide ions.

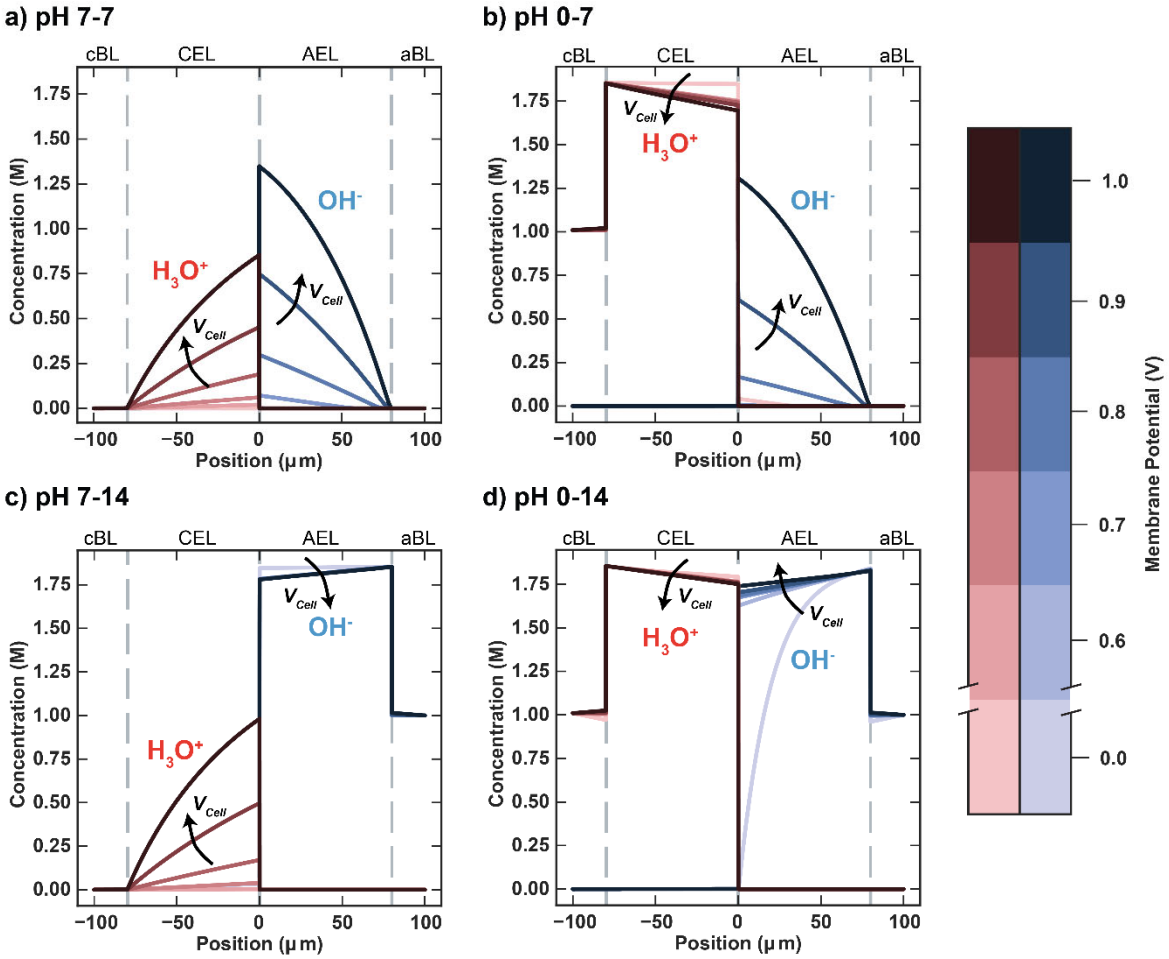

Figure 5: Hydronium and hydroxide concentration profiles at various applied potentials for four modeled pH environments. Arrows represent direction of increasing membrane potentials.

As demonstrated, the concentration profiles for hydronium and hydroxide are particularly pertinent to understanding multi-ion transport in a BPM because, when coupled with the electrostatic potential profiles, they elucidate the driving force for transport within each ion-exchange layer for a given electrolyte pairing. **Figure 6** depicts the relative contributions of diffusive transport ($-D_i \frac{dc_i}{dx}$) and migration ($z_i D_i c_i \frac{FE}{RT}$), in addition to contributions to transport due to water concentration gradients ($D_i c_i \frac{d(\ln(c_{H_2O}))}{dx}$), for the four applied pH gradients at a membrane potential of 0.8 V. In all cases, the fluxes of hydronium and hydroxide ions due to water

concentration gradients within the BPM is a small, but contributes in a non-negligible manner to the measured ionic current. Nonetheless, for ion-exchange layers in contact with a neutral electrolyte, the majority (~90 %) of the hydronium or hydroxide current density is carried by diffusion. This is expected due to the large concentration gradients that result from interfacial water dissociation. Conversely, for ion-exchange layers in contact with an acidic or alkaline electrolyte, the hydronium or hydroxide current is dominated by migration. In fact, for these cases, the driving force for diffusion opposes the reverse bias and must be overcome by the electrostatic potential driving force for migration. These conclusions demonstrate that there is a distinct change in the mechanism of transport for a BPM in a harsh applied pH gradient compared to what occurs for a BPM submersed in a neutral salt. This mechanistic change in BPM transport for very high or low pHs is vital towards understanding BPMs for electrolysis or electrosynthesis applications.

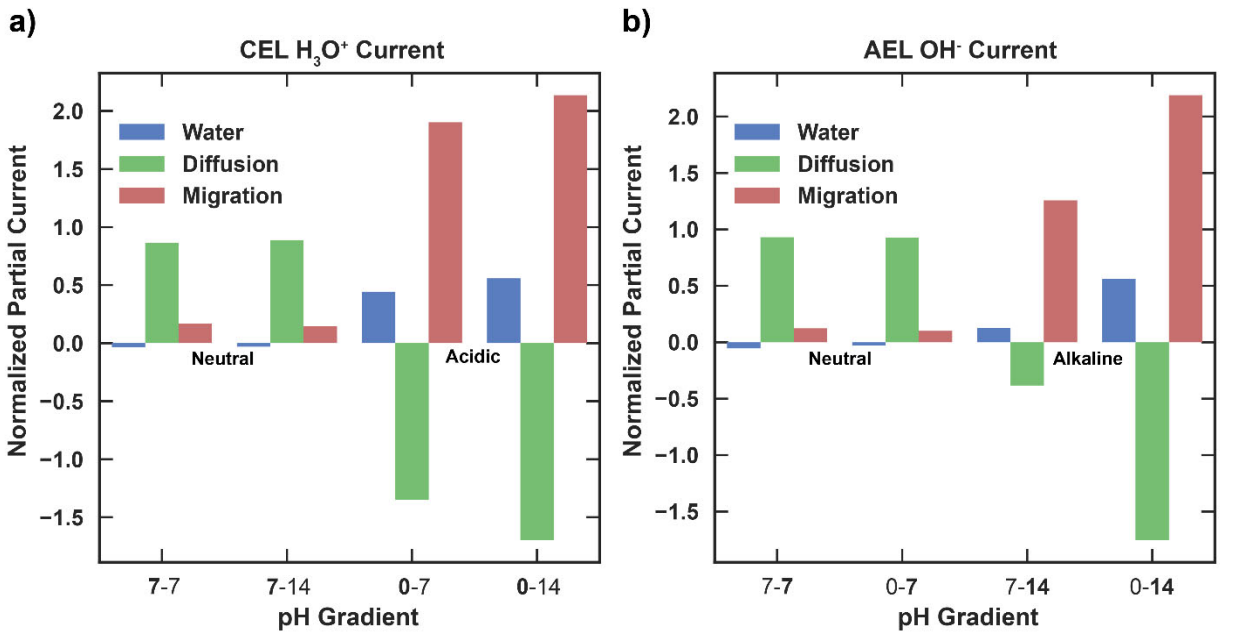

Figure 6: Breakdown of mechanistic contributions to (a) hydronium current in the CEL and (b) hydroxide current in the AEL at an applied potential of 0.8 V. All mechanistic partial currents are normalized by the total hydronium current or hydroxide current, respectively. Labels under bars display the neutrality, acidity, or alkalinity of the electrolyte adjacent to the given ion-exchange layer.

Key to the electrochemical characteristics of a BPM are the hydronium and hydroxide profiles at the interface between the AEL and the CEL. It is in this region, the electric field (Fig. S11) achieves its maximum and electroneutrality is broken (see **Figure 7**), thereby enabling the dissociation of water.[36,46,47] Mafé *et al.* predicted the formation of a "depletion zone" locally surrounding the AEL/CEL interface where there is an absence of mobile hydronium or hydroxide charges.[46] The analytical solution by Mafé also predicts that the double-layer thickness would be a function of membrane potential, and be between 2 to 10 nm.[46] This is shown in the simulated profiles (**Figure 7**). The double-layer is initially thinner than the catalyst layer, but as the applied potential increases, the thickness of the double-layer grows and eventually surpasses the catalyst layer thickness. Notably, the concentration peak for hydroxide in the double-layer is larger than that for hydronium. This is again due to the low diffusivity of hydroxide ions, as the hydronium ions can diffuse away from the double layer more rapidly. Interestingly, Fig. 6 reveals that the hydronium and hydroxide concentrations can reach values of ~1.85 M, exceeding the fixed-charge concentration of 1.81 M. This discrepancy is caused by the preservation of electroneutrality in the presence of salt ions outside of the double-layer. Therefore, these profiles are not only a function of the transport properties of hydronium and hydroxide ions, but also a function of other ions in the system. This finding reinforces the significance of understanding co- and counter-ion transport when modeling BPMs.

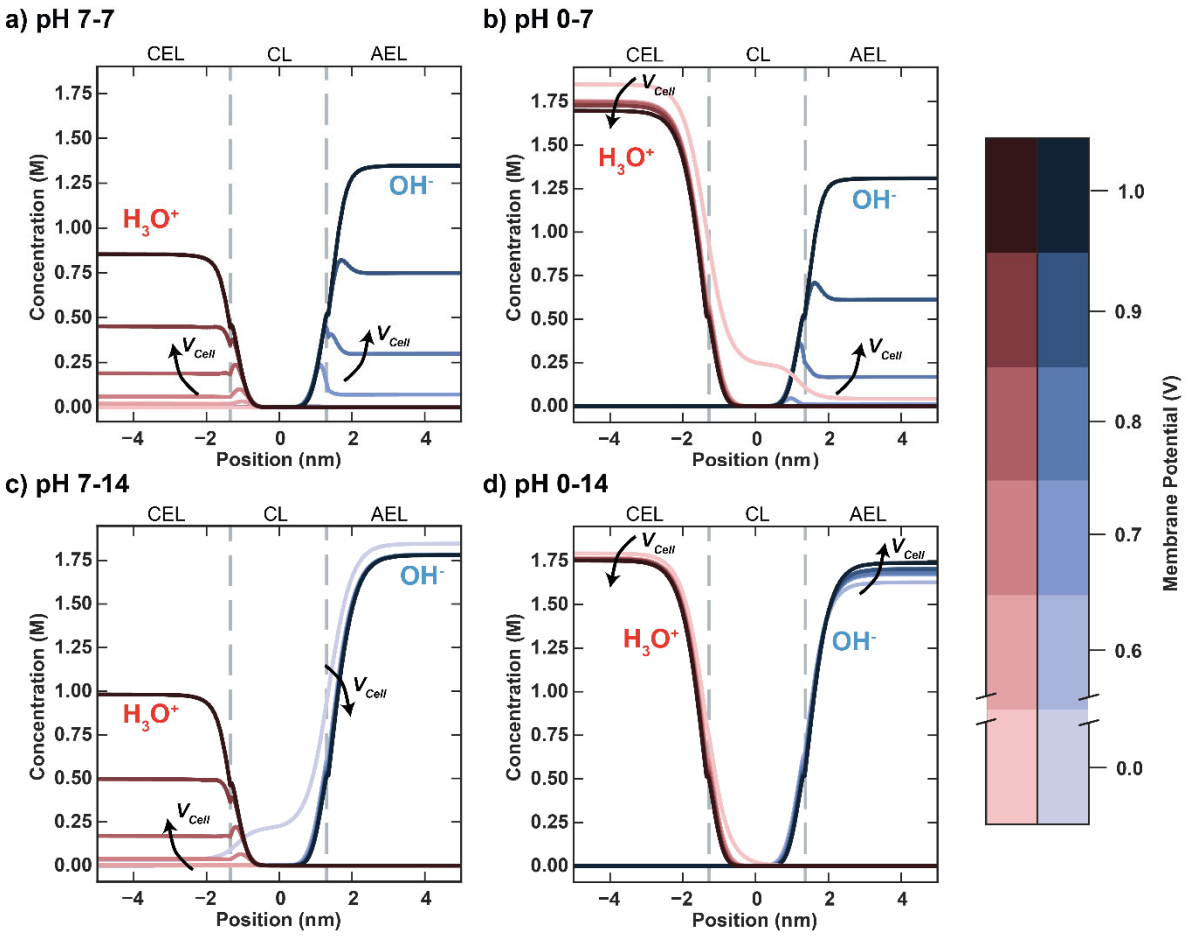

Figure 7: Hydronium and hydroxide concentration profiles in the depletion region at the AEL-CEL interface for various applied voltages in four modeled pH environments (zoomed-in plot of **Figure 5**). Arrows represent direction of increasing membrane potential.

3.4 Salt ion Transport and Impact of Buffer

To maintain steady pH gradients for electrolysis and improve membrane functionality, a complete understanding of how co- and counter-ion ions affect transport in a BPM is necessary. Several investigators have commented on the factors affecting co- and counter-ion transport. For example, Blommaert *et al.*[11] demonstrated that co- and counter-ion transport are affected by the equilibrium constant of the buffer reactions of the electrolyte species. Additionally, for other applications such as CO_2 electrolysis, which involves similar applied pH gradients, the electrolyte salt ion have been shown to have an impact on the reaction selectivity, with larger electrolyte cations suppressing

HER and improving CO_2 reduction selectivity.[78] Therefore, optimizing the choice of the electrolyte salt to maximize reaction efficiency and BPM performance is critical.

Insights into co- and counter-ion transport can be made by an analysis of species concentration profiles. At increased membrane potentials where breakdown occurs, the counter-ion profiles are opposite to those for hydronium and hydroxide ions and serve to maintain electroneutrality (Fig. S12, S13). For a reverse bias BPM, the counter-ions are in greatest concentration near the electrolyte due to Donnan effects and are minimal near the AEL/CEL junction where water dissociation occurs. Co-ions, on the other hand, are not as readily absorbed into the BPM due to Donnan exclusion and are thus present at low concentrations throughout the membrane.

While homogeneous buffer reactions are frequently neglected in models of BPMs, their impact must be taken into account. This is especially true in the pH 7-7 and pH 0-7 cases, for which the phosphate anions are strongly absorbed into the BPM due to direct contact of the phosphate-containing electrolyte with the AEL. For these environments, the AEL is initially saturated with phosphate species, and the buffer kinetics significantly affect the concentration profiles of the salt ions and the electrochemical characteristics of the BPM. **Figure 8** shows the polarization curves and AEL phosphate species profiles for the pH 7-7 and pH 0-7 cases with and without consideration of the homogeneous buffer equilibria for applied voltages within the salt ion-crossover regime. The polarization curves (**Figure 8a** and **Figure 8d**) exhibit significant changes when the homogeneous reaction equilibria are considered. Namely, the formation of a secondary plateau current is achieved when buffer equilibria are included in the model. Reference to the analysis of the partial current densities in the AEL presented in **Figure 4**, demonstrates that current in plateau region is carried primarily by the phosphate (green) species. This is further

supported by examining the concentration profiles (**Figure 8b** and **Figure 8e**), where the concentration profiles of phosphate species in the AEL reveals profiles that can explain the second phosphate plateau in the observed current. As the membrane potential is increased, hydroxide anions form within the catalyst layer and are transported into the AEL, thereby shifting the equilibrium between hydrogen phosphate and dihydrogen phosphate toward hydrogen phosphate (Eq. 10). This shift depresses the concentration of hydrogen phosphate and increases the concentration of dihydrogen phosphate in the AEL. As shown in **Figure 8c** and **Figure 8f**, when the buffer reactions are ignored, the concentration profiles within the AEL for phosphate remain linear, and no titration current is observed. Hence, to describe co- and counter-ion transport in a BPM fully, the homogeneous reaction equilibria must be considered.

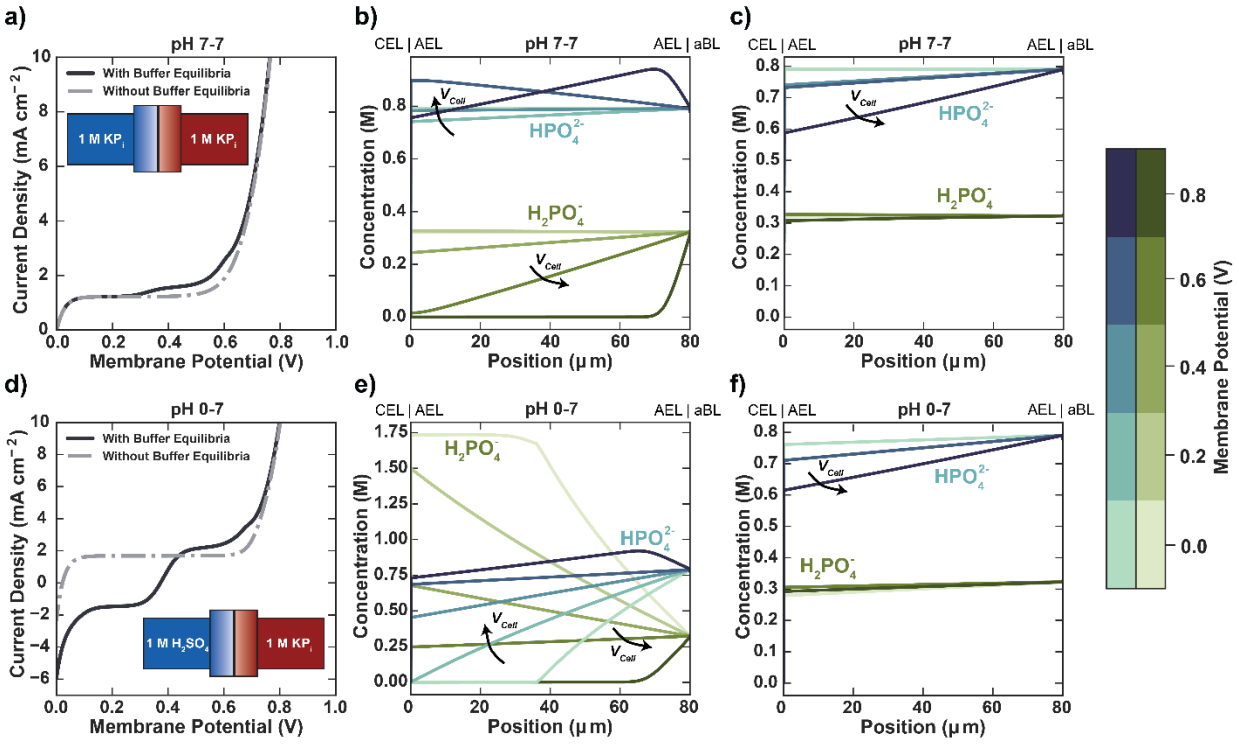

Figure 8: Polarization curves **(a,d)** and AEL phosphate concentration profiles with **(b,e)** and without **(c,f)** buffer equilibria for **(a-c)** pH 7-7 and pH 0-7 **(d-f).** Arrows represent direction of increasing membrane voltage.

Because the buffer equilibria affect BPM performance significantly, the choice of the anolyte species, which contains anions that readily transport into the AEL and undergo homogeneous reactions, is very important for developing a BPM-electrolyzer. To characterize the impact of the choice of anolyte species, polarization curves and partial current densities were analyzed for two additional electrolyte environments: 1 M HCl | 1 M Na_2SO_4 and 1 M HCl | 1 M $K_iH_jPO_4$ (**Figure 9**). Experimental methodology for the measurement of these polarization curves through 4-probe experiment is given in Section S6. These curves were fit using approximately the same fitting parameters used to fit the data of Vermaas *et al.*[10], except for very slight changes in the value of q (1.0 for Vermaas *et al.* to 1.1 for our data) and the catalyst effectiveness factor (1.8 for Vermaas *et al.* to 1.6 for our data). Notably, in the measurement of these polarization curves, the voltage at each applied current density was not recorded until the voltage stabilized to capture fully the steady-state behavior of the BPM (see Fig. S6.2). In both cases, the pH environment of the catholyte is 0 and that of the anolyte is 7. These electrolytes were chosen because, as shown in **Figure 8**, the current generated by titration for this pH environment is higher than for the pH 7-7 environment. The polarization curves for the two electrolyte combinations demonstrate that the choice of anolyte has a significant impact on the electrochemical characteristics of the BPM. While the kinetics of the water dissociation seem largely unaffected, and the magnitude of the salt-ion leakage currents are essentially identical, there is an observable difference in the open-circuit potential (OCP) of the two polarization curves. This is likely due to internal buffering within the bipolar membrane, as evidenced by the significant negative partial current densities of the buffered phosphate and sulfate species that can be attributed to titration currents. This is further supported by the fact that the OCPs in these two cases are proportional to the pK_a of their respective buffer

species. Further research should vary buffer species systematically over a variety of applied pH gradients, to examine fully the impact of the pK_a on the OCP of the BPM.

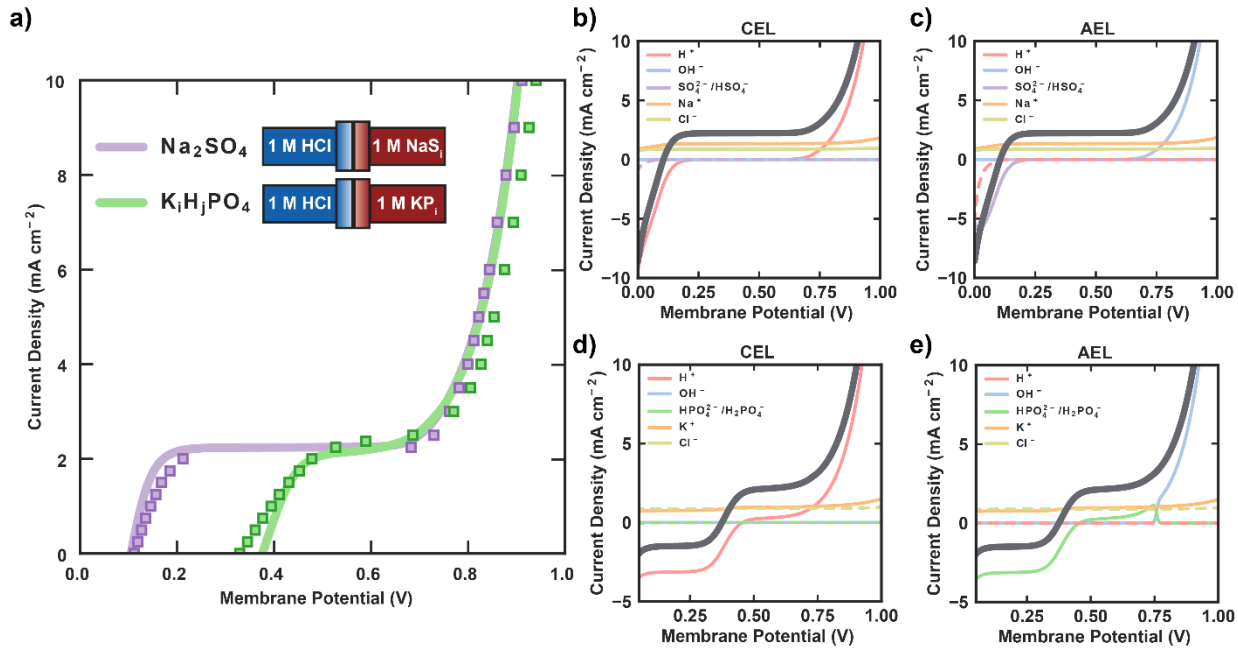

Figure 9: (a) Simulated (solid lines) and experimental (markers) polarization curves for pH 0-7 1 M HCl | 1 M Na_2SO_4 and 1 M HCl | 1 M $K_iH_jPO_4$ electrolytes. Partial-current-density breakdown in the **(b)** CEL and **(c)** AEL for a 1 M HCl | 1 M Na_2SO_4 submersed BPM. Partial current density breakdown in the **(d)** CEL and **(e)** AEL for a 1 M HCl | 1 M $K_iH_jPO_4$ submersed BPM.

3.5 Water Concentration Gradients

Controlling water transport within a BPM is critical to minimizing degradation of BPM-electrolyzer performance due to possible layer delamination caused by dehydration of the AEL/CEL junction at high current densities.[41,44,79] Therefore, maximizing BPM lifetime and performance requires knowledge of the water content and gradients in a BPM, something that has not previously been explored.[36,37] Prior studies by Crothers *et al.*[32] and Peng *et al.*[76] have demonstrated how ionomer hydration depends on the fraction of absorbed salt ions in a cationic- or an anionic-exchange membrane. Because of differences in osmotic pressure, as the fraction of co- or counter-ions in the membrane increases, the membrane takes up less water.[32] In other words, the salt ion-exchanged form of the AEL or CEL will take up less water than its corresponding

hydronium or hydroxide form. Work by Crothers *et al.*[32] has demonstrated that for most salt ions, the profile of hydration as a function or hydronium fraction in the CEL is approximately linear. Therefore, by fitting a value for the hydration of the AEL and CEL when completely exchanged with salt ions ($\lambda_{f_{H_3O^+}=0}, \lambda_{f_{OH^-}=0}$), the linear profile (Eq. 34-35) defining local ionomer hydration as a function of hydroxide or hydronium fraction captures approximately the decreased affinity for water in the two membranes with increasing salt ion uptake.

When concentration polarization is achieved in a BPM at high membrane potential in contact with a neutral electrolyte, there will be a distinct change in the majority carrier in the ion-exchange layer as the AEL/CEL junction is approached. Near the ionomer layer/electrolyte interfaces, the ionic concentration in the membrane is defined by Donnan equilibrium with the electrolyte, and the membrane strongly takes up counter-ions. However, near the AEL/CEL interface where dissociation occurs, the ion-exchange layers are exchanged by hydronium or hydroxide ions, respectively, due to local generation of these ions at high membrane potentials. Because membrane hydration depends on the specific ionic content of the membrane, the level of hydration is not uniform throughout the membrane, and there are internal gradients in water concentration (**Figure 10**). It is critical to capture these concentration gradients when modeling multi-ion transport because, as shown previously in **Figure 6**, they result in a non-negligible driving force for ionic current within the BPM. Also, sharp gradients in membrane hydration at the interface (see Figure S14) could lead to nonuniform swelling in the BPM that could, in turn, explain delamination due to dehydration.[31,77,80] Since the description of water transport within a BPM is incomplete, further work should seek to define more completely the effects of individual co- and counter-ions on membrane hydration. Also needed is a more thorough understanding of

water transport through the membrane in order to understand more fully the factors affecting membrane dry-out and delamination of BPMs.

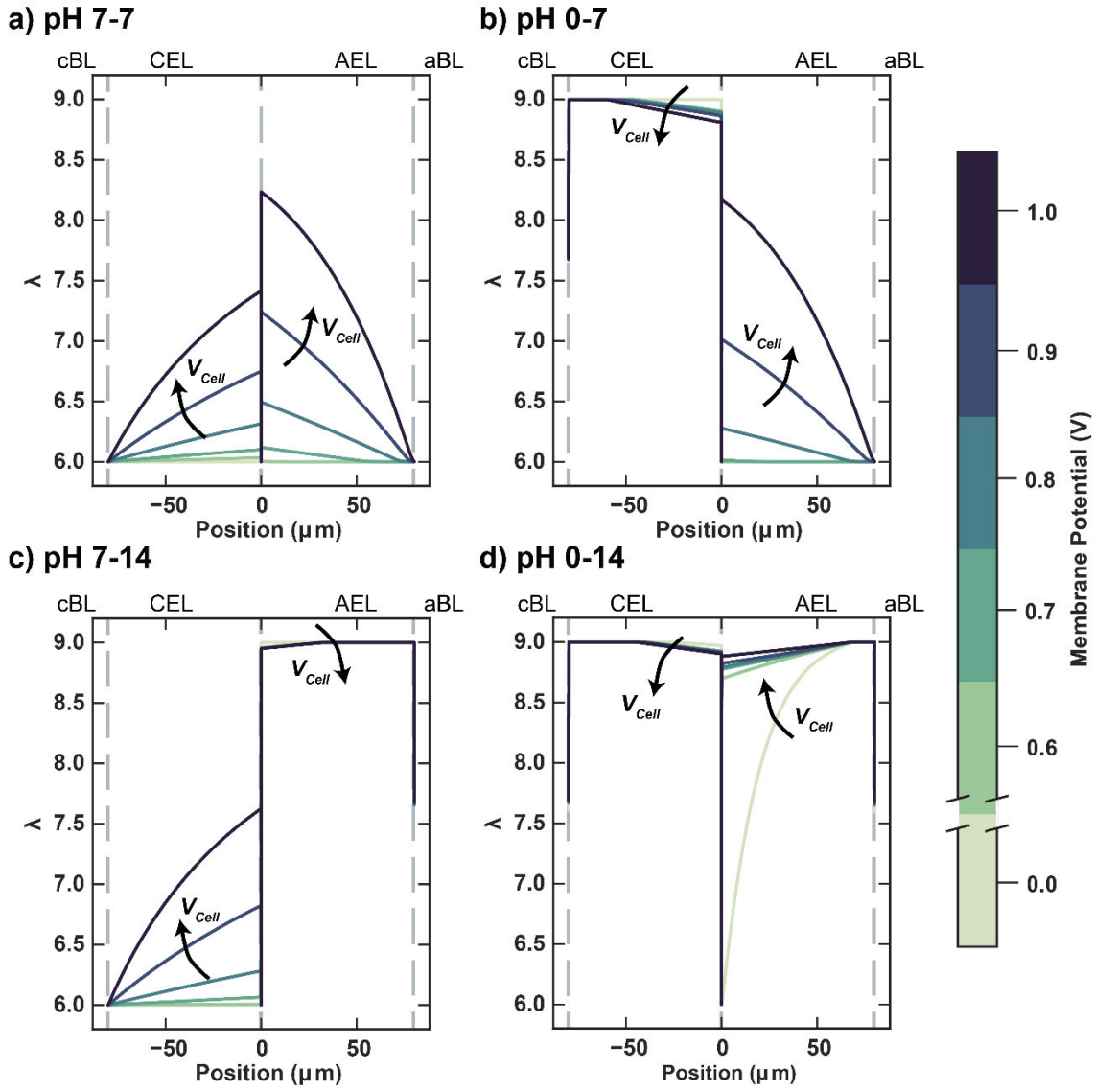

Figure 10: Water-content profiles at various applied potentials for four modeled pH environments. Arrows represent direction of increasing membrane potential.

3.6 Sensitivity Analysis

Although BPMs present great promise for application in electrolysis, until recently, they were primarily used for the generation of acid and base,[36,81–83] and, hence, there are only a handful of studies devoted to the design of next-generation BPMs for electrochemical technologies including

electrolyzers.[38,39,41] With this end in mind, we define two main objectives. First, the BPM must be able to achieve high current densities of water dissociation for minimal applied potentials. Second, the BPM should operate with minimal salt-ion crossover in order to maintain a stable pH gradient during extended operation. Using the developed model, we assess the parameter space for BPM design and provide recommendations for novel BPMs that are optimized for electrolysis. The sensitivity analysis discussed below was performed for the pH 7-7 polarization curve because it has the clearest delineation between the salt-ion crossover and water-dissociation regimes, enabling clearer visualization of the impact of the changes in parameters on co- and counter-ion leakage and water dissociation kinetics. Additionally, the low current densities simulated in this study are relevant for solar water splitting applications in similar near-neutral conditions. Furthermore, trends discovered for pH 7-7 translate well to the other pH gradients.

To achieve high water-dissociation current densities at lower applied potentials, it is necessary to optimize the water-dissociation catalysts in the BPM catalyst layer. In the current study, there are two parameters that control the behavior of the water dissociation catalyst: the catalyst-layer thickness, and the catalyst effectiveness factor, α. **Figure 11** shows the sensitivity of the model to these parameters. As shown in **Figure 11a**, a higher value of α and a thinner catalyst layer both decrease the onset potential required for breakdown and exhibit steeper slopes approaching the water-dissociation current density. By increasing α, the free energy of Bjerrum dipole is reduced and dissociation can occur more readily. Additionally, by decreasing the thickness of the catalyst layer, the catalyst is placed and utilized only near the center of the BPM, where the electric field is at its maximum. This increase in efficient utilization of the catalyst is responsible for the improvement in performance with a thinner catalyst layer, consistent with previous modeling studies.[37] Comparison to the values fit to the experimental data, L_{CL} = 2.7 nm

and α = 1.8 (see Table S8), demonstrates that there is room for improvement in the design of thinner, more effective water-dissociation catalyst layers, and **Figure 11** shows that the greatest opportunity for improvement is in using thinner catalyst layers.

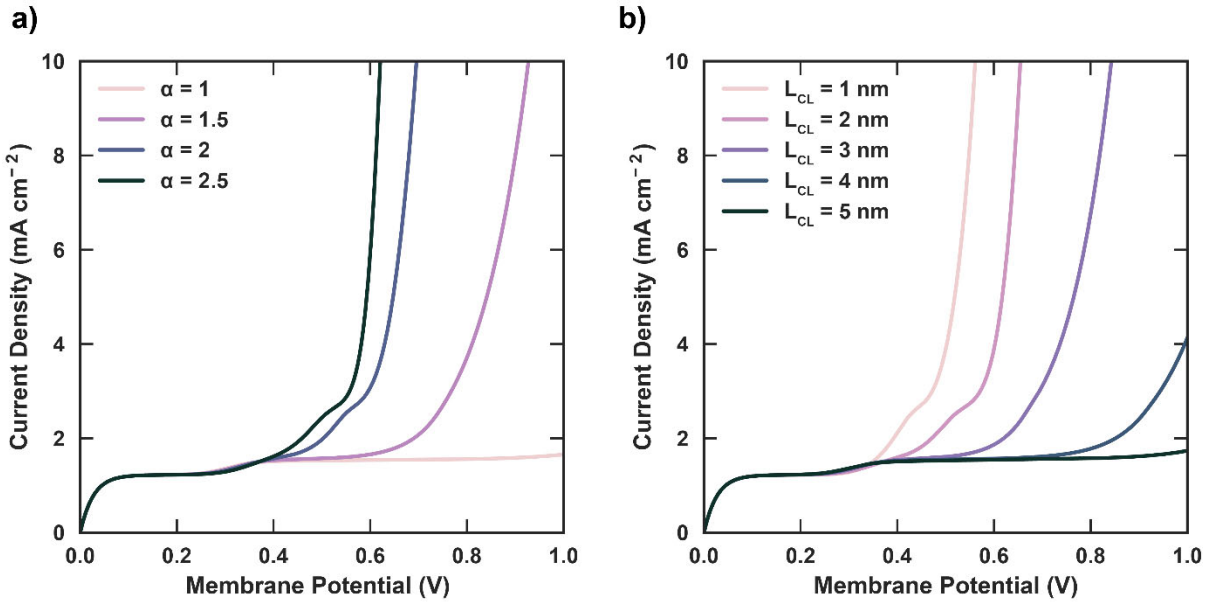

Figure 11: Modeled polarization curve for pH 7-7 for various **(a)** catalyst effectiveness factors and **(b)** catalyst-layer thicknesses. Fitted values for the BPM in the current study are L_{CL} = 2.7 nm and α = 1.8. (See Table S8)

At the high current densities required for commercial electrolysis (> 100 mA/cm^2),[1] the ohmic resistances in the membrane can lead to significant voltage losses. Therefore, it is desirable to reduce the thickness of the BPM in order to minimize ohmic overpotential losses at high water-dissociation current densities. However, reducing the thickness of the BPM will in turn increase the salt-ion leakage and reduce the stability of the applied pH gradient. Therefore, there is a tradeoff between ohmic losses and salt-ion leakage. This tradeoff is relevant to many electrochemical technologies,[84] and needs to be further explored for BPM devices. The effect of membrane thickness on the current/potential-characteristics of the BPM are shown in **Figure 12**. As expected, the co- and counter-ion leakage current observed increases with decreased membrane thickness. However, as evidenced by **Figure 12b-c**, the thickness of the AEL dictates the

magnitude of the salt-ion leakage, and the model is relatively insensitive to changes in the thickness of the CEL. Additionally, it is seen that the effects of decreasing the AEL and CEL independently are linearly additive (*i.e.* the sum of the change in leakage in **Figure 12b-c** equals the change in leakage in **Figure 12a)**. This implies that the most effective BPM would be one with as thin a CEL as possible supported on a thicker AEL in order to keep salt-ion leakage low and membrane conductance high, while maintaining mechanical integrity. This type of asymmetric BPM-structure has been proposed for BPM CO_2 electrolysis, where a thinner, porous CEL allows for any CO_2 gas formed at the AEL/CEL junction to permeate back to the cathode where it could be utilized.[44]

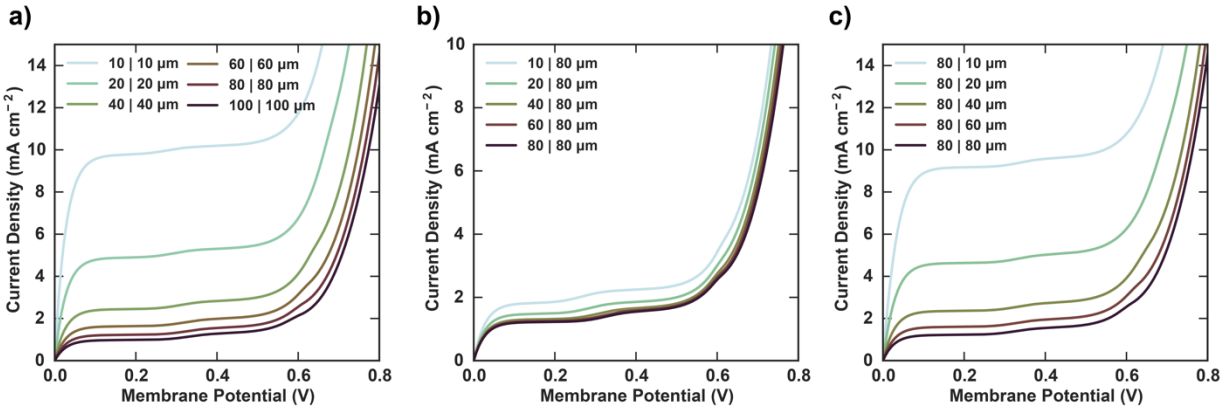

Figure 12: Effect of modifying BPM membrane thickness **(a)** symmetrically, **(b)** of just the CEL, and **(c)** of just the AEL. Membrane used in study was symmetric with an 80 µm CEL and an 80 µm AEL.

The last set of parameters that can be optimized in the BPM are those related to the physical properties of the ionomer layers: the membrane water uptake and the IEC. These are related in that the water uptake increases with IEC for ionomers.[31,85] Nonetheless, for the purposes of the sensitivity analysis, it is elucidating to modulate them separately. Prior studies have shown that the Fumasep BPMs exhibit drastically lower water uptake ($\lambda = 9$)[11] than commercial monopolar membranes like Nafion ($\lambda = 21$)[77,86] or Tokuyama A201 ($\lambda = 17$) .[76] For these monopolar

membranes there is an incentive to maximize water uptake in order to improve conductivity and prevent membrane dehydration. However, BPMs face another trade-off. As shown in **Figure 13a**, increased water uptake severely increases salt-ion leakage due to the dependence on the transport coefficients of the salt ions on the water content within the BPM. At the Nafion hydration of 21, the BPM exhibits a significant (~30 mA cm^{-2}) of co- and counter-ion leakage current. Therefore, the high hydration of commercial monopolar membranes will be undesirable in the fabrication of BPMs; consequently, further work should seek to find an optimum balance between membrane hydration and salt-ion leakage. When exploring methods to minimize crossover current and membrane resistance in the context of redox flow batteries, Crothers *et al.* found that one approach to achieving optimum performance was to change the transport coefficient or uptake of ions in the membrane by making the redox species much larger or to change the membrane pore size to more closely match the size of the redox species to leverage size-exclusion properties.[84] Future modeling efforts should attempt to capture size-exclusion effects and membrane-species interactions in order to study the sensitivity of salt-ion crossover to these parameters.

While the effect of increased water uptake is quite straightforward, the impact of increasing IEC, which characterizes the amount of membrane fixed charge groups per gram of membrane, is complex. In **Figure 13b**, it is observed that as the IEC is increased, the salt-ion leakage increases, a result that is detrimental to performance, but the applied potential required for breakdown is reduced, implying an improvement in water-dissociation kinetics. Both effects are coupled to the increase in fixed-charge concentration in the membrane that corresponds to an increase in the IEC. As the fixed-charge concentration increases, the water uptake and number of ions that transport into the membrane by Donnan equilibrium increases, leading to an increase in salt-ion leakage. Additionally, increasing IEC could lead to higher likelihood of mechanical breakdown, because

all ions will be more readily solvated and dissolved.[31] At the same time, increasing the magnitude of fixed charges in each exchange layer increases the gradient in fixed-charge density at the AEL/CEL junction, leading to a larger local electric field and thus enhanced water dissociation for higher IECs due to the Second Wien Effect. The coupled sensitivity of the IEC to enhancements in water dissociation and increases in co- and counter-ion leakage makes it difficult to optimize the IEC for a BPM. Since the sensitivity of the salt-ion leakage current is minimal, the electric-field enhancement will likely be more critical to defining the BPM performance at high current densities desired for electrolysis.[1,11] Therefore, it is sensible to maximize the IEC in order to enhance interfacial water dissociation, although there is an intrinsic limit where the ionomer will dissolve at high enough IECs.

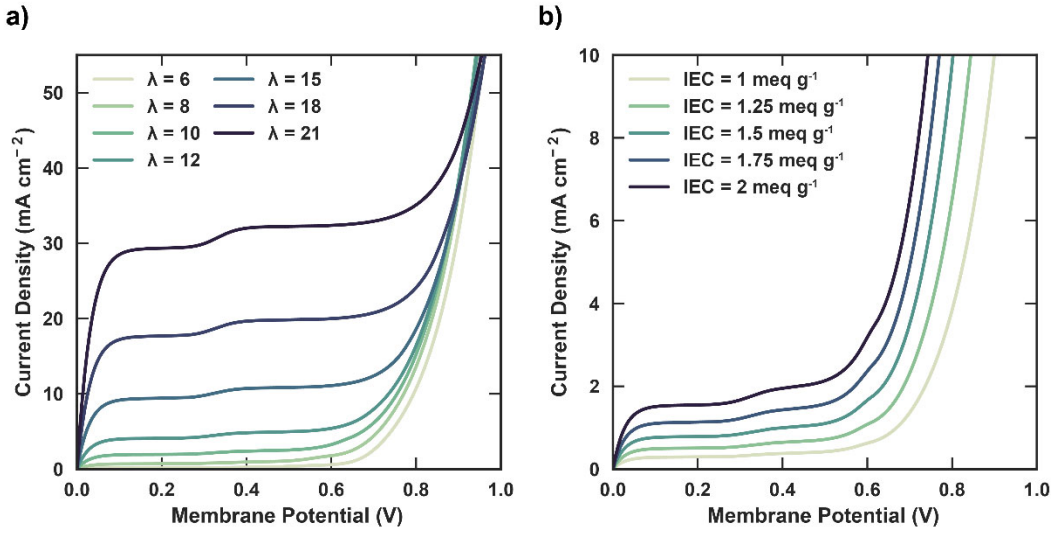

Figure 13: Effect of modifying **(a)** BPM hydration and **(b)** ion-exchange capacity. BPM hydration in study had a λ of 9 and an IEC of 1.81 meq g^{-1}.

Conclusions

A comprehensive model for a bipolar membrane (BPM) operated in reverse bias was developed and validated against experimental data. The model accounts for the effects of multi-ion transport, homogeneous reaction kinetics, electric field-dependent water dissociation, and catalyzed water-

dissociation kinetics. Simulations based on this model describe previously unexplained electrochemical phenomena such as internal concentration polarization and salt ion crossover that are critical for developing energy efficient and pH stable BPM-electrolyzers. The model also demonstrates several important phenomena central to multi-ion transport within the BPM. In particular, the simulations reveal that co- and counter-ion currents dominate at low current densities, that there is a distinct change in the mode of transport between diffusion for a BPM in a neutral electrolyte and migration for a BPM in a highly alkaline or acidic electrolyte, and that the buffer kinetics of the electrolyte salt ions are vital for describing co- and counter-ion crossover fully in a BPM. Lastly, the model demonstrates the sensitivity of BPM performance to the catalyst-layer properties and physical properties of the ion-exchange layers. The simulations show that an optimal BPM should have a thin dissociation catalyst layer, and a thinner AEM than CEM layer in order to manage water transport, control salt-ion crossover, and ameliorate ohmic resistance. The work reported also identifies areas for improving that the accuracy of the model for a BPM. These include capturing concentrated-solution effects, membrane/species interactions, and solving explicitly for water transport. These phenomena will become especially relevant at current densities higher than those currently measured experimentally but relevant for device operation. Nevertheless, the results of the present study provide information that is critical to developing a comprehensive understanding of multi-ion transport in BPMs and informs the design and implementation of BPMs in next-generation devices for various electrochemical reactions that benefit from operation under an applied pH gradient.

Acknowledgements

This material is based upon work performed at the Joint Center for Artificial Photosynthesis, a DOE Energy Innovation Hub, supported through the Office of Science of the U.S. Department of Energy under Award Number DE-SC0004993 and the National Institutes of Health under Grant No. S10OD023532. JCB acknowledges funding from the National Science Foundation Graduate Research Fellowship under Grant No. DGE 1752814. The authors would also like to thank David Vermaas, Philomena Weng, and Andrew Crothers for insightful and fruitful discussions regarding the nature of ionic transport in bipolar membranes.

Nomenclature

Roman

c_i	Concentration of species i (M)
D_i	Diffusivity of species i (m^2 s^{-1})
E	Electric field (V m^{-1})
E	Elementary charge
F	Faraday's constant
G	Gibb's Free Energy (J mol^{-1})
IEC	Ion Exchange capacity (mmol g^{-1})
k_B	Boltzmann's constant
K_n	Equilibrium constant in reaction n
K_n	Forward rate constant of reaction n
L	Length m
l_B	Bjerrum Length
M_i	Molar mass of species i
N_i	Molar flux of species i
R	Ideal gas constant
R_i	Source term for species i
$s_{i,n}$	Stoichiometric coefficient of species i in reaction n
T	Temperature
x	1-dimensional position variable
z_i	Charge of ion i

Greek

α	Catalyst effectiveness factor
β	Non-dimensional electric field
γ_i	Activity coefficient of species i
ε	Dielectric permittivity (F m^{-1})
λ	Water content
μ	Chemical potential of species i
ξ	Species-membrane/Species-water diffusivity ratio
ρ	Density (g cm^{-3})
σ	Dimensionless dissociation bond length
Φ	Electrostatic potential
ϕ	Ionomer water volume fraction

Subscript

$-$	Hydroxide species
$+$	Hydronium species
$char$	Characteristic
eff	Effective
i	Ionic species
w	Value in water

Superscript

0	Intrinsic value or standard state
E	Electric field dependence

Acronyms

aBL	Anolyte Boundary Layer
AEL	Anion Exchange Layer
BPM	Bipolar Membrane
cBL	Catholyte Boundary Layer
CEL	Cation Exchanger Layer
CL	Catalyst Layer
DL	Double-Layer

For Table of Contents Only

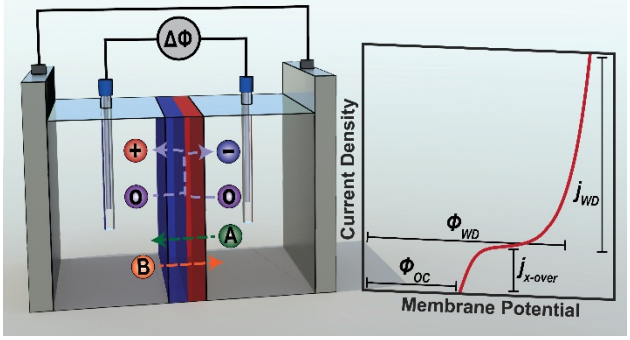

References

(1) Barbir, F. PEM Electrolysis for Production of Hydrogen from Renewable Energy Sources. *Sol. Energy* **2005**, *78*, 661–669. https://doi.org/10.1016/j.solener.2004.09.003.

(2) Mazloomi, K.; Gomes, C. Hydrogen as an Energy Carrier: Prospects and Challenges. *Renew. Sustain. Energy Rev.* **2012**, *16* (5), 3024–3033. https://doi.org/10.1016/j.rser.2012.02.028.

(3) Blanco, D. E.; Modestino, M. A. Organic Electrosynthesis for Sustainable Chemical Manufacturing. *Trends Chem.* **2019**, *1* (1), 8–10. https://doi.org/10.1016/j.trechm.2019.01.001.

(4) Kumari, S.; Turner White, R.; Kumar, B.; Spurgeon, J. M. Solar Hydrogen Production from Seawater Vapor Electrolysis. *Energy Environ. Sci.* **2016**, *9* (5), 1725–1733. https://doi.org/10.1039/C5EE03568F.

(5) Dai, W.; Wang, H.; Yuan, X. Z.; Martin, J. J.; Yang, D.; Qiao, J.; Ma, J. A Review on Water Balance in the Membrane Electrode Assembly of Proton Exchange Membrane Fuel Cells. *Int. J. Hydrogen Energy* **2009**, *34* (23), 9461–9478. https://doi.org/10.1016/j.ijhydene.2009.09.017.

(6) Weng, L. C.; Bell, A. T.; Weber, A. Z. Towards Membrane-Electrode Assembly Systems for CO2 Reduction: A Modeling Study. *Energy Environ. Sci.* **2019**, *12* (6), 1950–1968. https://doi.org/10.1039/c9ee00909d.

(7) Blanco, D. E.; Prasad, P. A.; Dunningan, K.; Modestino, M. A. Insights into Membrane-Separated Organic Electrosynthesis: The Case of Adiponitrile Electrochemical

Production. *React. Chem. Eng.* **2020**, *5* (1), 136–144. https://doi.org/10.1039/c9re00389d.

(8) Salvatore, D. A.; Weekes, D. M.; He, J.; Dettelbach, K. E.; Li, Y. C.; Mallouk, T. E.; Berlinguette, C. P. Electrolysis of Gaseous CO2 to CO in a Flow Cell with a Bipolar Membrane. *ACS Energy Lett.* **2018**, *3* (1), 149–154. https://doi.org/10.1021/acsenergylett.7b01017.

(9) Li, Y. C.; Zhou, D.; Yan, Z.; Gonçalves, R. H.; Salvatore, D. A.; Berlinguette, C. P.; Mallouk, T. E. Electrolysis of CO2 to Syngas in Bipolar Membrane-Based Electrochemical Cells. *ACS Energy Lett.* **2016**, *1* (6), 1149–1153. https://doi.org/10.1021/acsenergylett.6b00475.

(10) Vermaas, D. A.; Wiegman, S.; Smith, W. A. Ion Transport Mechanisms in Bipolar Membranes for (Photo)Electrochemical Water Splitting. *Sustain. Energy Fuels* **2018**, No. 9, 2006–2015. https://doi.org/10.1039/c8se00118a.

(11) Blommaert, M. A.; Verdonk, J. A. H.; Blommaert, H. C. B.; Smith, W. A.; Vermaas, D. A. Reduced Ion Crossover in Bipolar Membrane Electrolysis via Increased Current Density, Molecular Size and Valence. *ACS Appl. Energy Mater.* **2020**, *Just Accep*. https://doi.org/10.1021/acsaem.0c00687.

(12) Vermaas, D. A.; Smith, W. A. Synergistic Electrochemical CO2 Reduction and Water Oxidation with a Bipolar Membrane. *ACS Energy Lett.* **2016**, *1* (6), 1143–1148. https://doi.org/10.1021/acsenergylett.6b00557.

(13) Carmo, M.; Fritz, D. L.; Mergel, J.; Stolten, D. A Comprehensive Review on PEM Water Electrolysis. *Int. J. Hydrogen Energy* **2013**, *38* (12), 4901–4934.

https://doi.org/10.1016/j.ijhydene.2013.01.151.

(14) Buttler, A.; Spliethoff, H. Current Status of Water Electrolysis for Energy Storage, Grid Balancing and Sector Coupling via Power-to-Gas and Power-to-Liquids: A Review. *Renew. Sustain. Energy Rev.* **2018**, *82* (September 2017), 2440–2454. https://doi.org/10.1016/j.rser.2017.09.003.

(15) Holladay, J. D.; Hu, J.; King, D. L.; Wang, Y. An Overview of Hydrogen Production Technologies. *Catal. Today* **2009**, *139* (4), 244–260. https://doi.org/10.1016/j.cattod.2008.08.039.

(16) Shaner, M. R.; Atwater, H. A.; Lewis, N. S.; McFarland, E. W. A Comparative Technoeconomic Analysis of Renewable Hydrogen Production Using Solar Energy. *Energy Environ. Sci.* **2016**, *9* (7), 2354–2371. https://doi.org/10.1039/C5EE02573G.

(17) McCrory, C. C. L.; Jung, S.; Ferrer, I. M.; Chatman, S. M.; Peters, J. C.; Jaramillo, T. F. Benchmarking Hydrogen Evolving Reaction and Oxygen Evolving Reaction Electrocatalysts for Solar Water Splitting Devices. *J. Am. Chem. Soc.* **2015**, *137* (13), 4347–4357. https://doi.org/10.1021/ja510442p.

(18) Siracusano, S.; Van Dijk, N.; Payne-Johnson, E.; Baglio, V.; Aricò, A. S. Nanosized IrOx and IrRuOx Electrocatalysts for the O2 Evolution Reaction in PEM Water Electrolysers. *Appl. Catal. B Environ.* **2015**, *164*, 488–495. https://doi.org/10.1016/j.apcatb.2014.09.005.

(19) Shaner, M. R.; Atwater, H. A.; Lewis, N. S.; McFarland, E. W. A Comparative Technoeconomic Analysis of Renewable Hydrogen Production Using Solar Energy. *Energy Environ. Sci.* **2016**, *9* (7), 2354–2371. https://doi.org/10.1039/c5ee02573g.

(20) Lazouski, N.; Chung, M.; Williams, K.; Gala, M. L.; Manthiram, K. Non-Aqueous Gas Diffusion Electrodes for Rapid Ammonia Synthesis from Nitrogen and Water-Splitting-Derived Hydrogen. *Nat. Catal.* **2020**, *3* (May). https://doi.org/10.1038/s41929-020-0455-8.

(21) Blanco, D. E.; Dookhith, A. Z.; Modestino, M. A. Enhancing Selectivity and Efficiency in the Electrochemical Synthesis of Adiponitrile. *React. Chem. Eng.* **2019**, *4* (1), 8–16. https://doi.org/10.1039/c8re00262b.

(22) Basumatary, P.; Konwar, D.; Yoon, Y. S. Conductivity-Tailored PtNi/MoS2 3D Nanoflower Catalyst via Sc Doping as a Hybrid Anode for a Variety of Hydrocarbon Fuels in Proton Exchange Membrane Fuel Cells. *Appl. Catal. B Environ.* **2020**, *267*, 118724. https://doi.org/10.1016/j.apcatb.2020.118724.

(23) Walter, M. G.; Warren, E. L.; McKone, J. R.; Boettcher, S. W.; Mi, Q.; Santori, E. A.; Lewis, N. S. Solar Water Splitting Cells. *Chem. Rev. (Washington, DC, United States)* **2010**, *110* (11), 6446–6473. https://doi.org/10.1021/cr1002326.

(24) Gratzel, M. Photoelectrochemical Cells. *Nature* **2001**, *414*, 338–344. https://doi.org/10.1016/S0140-6736(06)68542-5.

(25) Luo, J.; Vermaas, D. A.; Bi, D.; Hagfeldt, A.; Smith, W. A.; Grätzel, M. Bipolar Membrane-Assisted Solar Water Splitting in Optimal PH. *Adv. Energy Mater.* **2016**, *6* (13), 1–7. https://doi.org/10.1002/aenm.201600100.

(26) Oener, S. Z.; Ardo, S.; Boettcher, S. W. Ionic Processes in Water Electrolysis: The Role of Ion-Selective Membranes. *ACS Energy Lett.* **2017**, *2* (11), 2625–2634.

https://doi.org/10.1021/acsenergylett.7b00764.

(27) Xiang, C.; Papadantonakis, K. M.; Lewis, N. S. Principles and Implementations of Electrolysis Systems for Water Splitting. *Mater. Horizons* **2016**, *3* (3), 169–173. https://doi.org/10.1039/c6mh00016a.

(28) Sun, K.; Liu, R.; Chen, Y.; Verlage, E.; Lewis, N. S.; Xiang, C. A Stabilized , Intrinsically Safe , 10 % Effi Cient , Solar- Driven Water-Splitting Cell Incorporating Earth-Abundant Electrocatalysts with Steady-State PH Gradients and Product Separation Enabled by a Bipolar Membrane COMMUNICATION. *Adv. Energy Mater.* **2016**, No. 6, 1–7. https://doi.org/10.1002/aenm.201600379.

(29) Mcdonald, M. B.; Ardo, S.; Lewis, N. S.; Freund, M. S. Use of Bipolar Membranes for Maintaining Steady-State PH Gradients in Membrane-Supported , Solar-Driven Water Splitting. *ChemSusChem* **2014**, No. 7, 3021–3027. https://doi.org/10.1002/cssc.201402288.

(30) Xiang, C.; Weber, A. Z.; Ardo, S.; Berger, A.; Chen, Y.; Coridan, R.; Fountaine, K. T.; Haussener, S.; Hu, S.; Liu, R.; Lewis, N. S.; Modestino, M. A.; Shaner, M. M.; Singh, M. R.; Stevens, J. C.; Sun, K.; Walczak, K. Modeling , Simulation , and Implementation of Solar- Driven Water-Splitting Devices Angewandte. *Angew. Chemie* **2016**, No. 55, 12974–12988. https://doi.org/10.1002/anie.201510463.

(31) Kusoglu, A.; Weber, A. Z. New Insights into Perfluorinated Sulfonic-Acid Ionomers. *Chem. Rev.* **2017**, *117* (3), 987–1104. https://doi.org/10.1021/acs.chemrev.6b00159.

(32) Crothers, A. R.; Darling, R. M.; Kusoglu, A.; Radke, C. J.; Weber, A. Z. Theory of

Multicomponent Phenomena in Cation-Exchange Membranes: Part I. Thermodynamic Model and Validation. *J. Electrochem. Soc.* **2020**, *167* (1), 013547. https://doi.org/10.1149/1945-7111/ab6723.

(33) Schaberg, M. S.; Abulu, J. E.; Haugen, G. M.; Emery, M. A.; O'Conner, S. J.; Xiong, P. N.; Hamrock, S. J. New Multi Acid Side-Chain Ionomers for Proton Exchange Membrane Fuel Cells. *ECS Trans.* **2010**, *33* (1), 627–633.

(34) Qiu, B.; Lin, B.; Qiu, L.; Yan, F. Alkaline Imidazolium- and Quaternary Ammonium-Functionalized Anion Exchange Membranes for Alkaline Fuel Cell Applications. *J. Mater. Chem.* **2012**, *22* (3), 1040–1045. https://doi.org/10.1039/c1jm14331j.

(35) Kutz, R. B.; Chen, Q.; Yang, H.; Sajjad, S. D.; Liu, Z.; Masel, I. R. Sustainion Imidazolium-Functionalized Polymers for Carbon Dioxide Electrolysis. *Energy Technol.* **2017**, *5* (6), 929–936. https://doi.org/10.1002/ente.201600636.

(36) Craig, N. P. Electrochemical Behavior of Bipolar Membranes. **2013**.

(37) Mareev, S. A.; Evdochenko, E.; Wessling, M.; Kozaderova, O. A.; Niftaliev, S. I.; Pismenskaya, N. D.; Nikonenko, V. V. A Comprehensive Mathematical Model of Water Splitting in Bipolar Membranes: Impact of the Spatial Distribution of Fixed Charges and Catalyst at Bipolar Junction. *J. Memb. Sci.* **2020**, *603*, 118010. https://doi.org/10.1016/j.memsci.2020.118010.

(38) McDonald, M. B.; Freund, M. S. Graphene Oxide as a Water Dissociation Catalyst in the Bipolar Membrane Interfacial Layer. *ACS Appl. Mater. Interfaces* **2014**, *6* (16), 13790–13797. https://doi.org/10.1021/am503242v.

(39) McDonald, M. B.; Freund, M. S.; Hammond, P. T. Catalytic, Conductive Bipolar Membrane Interfaces through Layer-by-Layer Deposition for the Design of Membrane-Integrated Artificial Photosynthesis Systems. *ChemSusChem* **2017**, *10* (22), 4599–4609. https://doi.org/10.1002/cssc.201701397.

(40) McDonald, M. B.; Bruce, J. P.; McEleney, K.; Freund, M. S. Reduced Graphene Oxide Bipolar Membranes for Integrated Solar Water Splitting in Optimal PH. *ChemSusChem* **2015**, *8* (16), 2645–2654. https://doi.org/10.1002/cssc.201500538.

(41) Shen, C.; Wycisk, R.; Pintauro, P. N. High Performance Electrospun Bipolar Membrane with a 3D Junction. *Energy Environ. Sci.* **2017**, *10* (6), 1435–1442. https://doi.org/10.1039/c7ee00345e.

(42) Oener, S. Z.; Foster, M. J.; Boettcher, S. W. Accelerating Water Dissociation in Bipolar Membranes and for Electrocatalysis. *Science (80-.).* **2020**, eaaz1487. https://doi.org/10.1126/science.aaz1487.

(43) Gabrielsson, E. O.; Tybrandt, K.; Berggren, M. Ion Diode Logics for PH Control. *Lab Chip* **2012**, *12* (14), 2507–2513. https://doi.org/10.1039/c2lc40093f.

(44) Patru, A.; Binninger, T.; Pribyl, B.; Schmidt, T. J. Design Principles of Bipolar Electrochemical Co-Electrolysis Cells for Efficient Reduction of Carbon Dioxide from Gas Phase at Low Temperature. *J. Electrochem. Soc.* **2019**, *166* (2), F34–F43. https://doi.org/10.1149/2.1221816jes.

(45) White, W.; Sanborn, C. D.; Fabian, D. M.; Ardo, S. Conversion of Visible Light into Ionic Power Using Photoacid-Dye-Sensitized Bipolar Ion-Exchange Membranes. *Joule* **2018**, *2*

(1), 94–109. https://doi.org/10.1016/j.joule.2017.10.015.

(46) Mafé, S.; Ramfaz, P. Electrochemical Characterization of Polymer Ion-Exchange Bipolar Membranes. *Acta Polym.* **1997**, *48* (7), 234–250. https://doi.org/10.1002/actp.1997.010480702.

(47) Mafé, S.; Ramírez, P.; Alcaraz, A. Electric Field-Assisted Proton Transfer and Water Dissociation at the Junction of a Fixed-Charge Bipolar Membrane. *Chem. Phys. Lett.* **1998**, *294* (4–5), 406–412. https://doi.org/10.1016/S0009-2614(98)00877-X.

(48) Yan, Z.; Zhu, L.; Li, Y. C.; Wycisk, R. J.; Pintauro, P. N.; Hickner, M. A.; Mallouk, T. E. The Balance of Electric Field and Interfacial Catalysis in Promoting Water Dissociation in Bipolar Membranes. *Energy Environ. Sci.* **2018**, *11* (8), 2235–2245. https://doi.org/10.1039/c8ee01192c.

(49) Vermaas, D. A.; Sassenburg, M.; Smith, W. A. Photo-Assisted Water Splitting with Bipolar Membrane Induced PH Gradients for Practical Solar Fuel Devices. *J. Mater. Chem. A* **2015**, *3* (38), 19556–19562. https://doi.org/10.1039/c5ta06315a.

(50) Vargas-Barbosa, N. M.; Geise, G. M.; Hickner, M. A.; Mallouk, T. E. Assessing the Utility of Bipolar Membranes for Use in Photoelectrochemical Water-Splitting Cells. *ChemSusChem* **2014**, *7* (11), 3017–3020. https://doi.org/10.1002/cssc.201402535.

(51) Chabi, S.; Wright, A. G.; Holdcroft, S.; Freund, M. S. Transparent Bipolar Membrane for Water Splitting Applications. *ACS Appl. Mater. Interfaces* **2017**, acsami.7b04402. https://doi.org/10.1021/acsami.7b04402.

(52) Hurwitz, H. D.; Dibiani, R. Experimental and Theoretical Investigations of Steady and

Transient States in Systems of Ion Exchange Bipolar Membranes. *J. Memb. Sci.* **2004**, *228* (1), 17–43. https://doi.org/10.1016/j.memsci.2003.09.009.

(53) Ramírez, P.; Rapp, H. J.; Reichle, S.; Strathmann, H.; Mafé, S. Current-Voltage Curves of Bipolar Membranes. *J. Appl. Phys.* **1992**, *72* (1), 259–264. https://doi.org/10.1063/1.352124.

(54) Schiffbauer, J.; Ganchenko, N. Y.; Ganchenko, G. S.; Demekhin, E. A. Overlimiting Current Due to Electro-Diffusive Amplification of the Second Wien Effect at a Cation-Anion Bipolar Membrane Junction. *Biomicrofluidics* **2018**, *12* (6). https://doi.org/10.1063/1.5066195.

(55) Volgin, V. M.; Davydov, A. D. Ionic Transport through Ion-Exchange and Bipolar Membranes. *J. Memb. Sci.* **2005**, *259* (1–2), 110–121. https://doi.org/10.1016/j.memsci.2005.03.010.

(56) Conroy, D. T.; Craster, R. V.; Matar, O. K.; Cheng, L. J.; Chang, H. C. Nonequilibrium Hysteresis and Wien Effect Water Dissociation at a Bipolar Membrane. *Phys. Rev. E - Stat. Nonlinear, Soft Matter Phys.* **2012**, *86* (5). https://doi.org/10.1103/PhysRevE.86.056104.

(57) Strathmann, H.; Krol, J. J.; Rapp, H. J.; Eigenberger, G. Limiting Current Density and Water Dissociation in Bipolar Membranes. *J. Memb. Sci.* **1997**, *125* (1), 123–142. https://doi.org/10.1016/S0376-7388(96)00185-8.

(58) Crothers, A. R.; Darling, R. M.; Kusoglu, A.; Radke, C. J.; Weber, A. Z. Theory of Multicomponent Phenomena in Cation-Exchange Membranes: Part II. Transport Model

and Validation. *J. Electrochem. Soc.* **2020**, *167* (1), 013548. https://doi.org/10.1149/1945-7111/ab6724.

(59) Fumatech. Technical Data Sheet for Fumasep FBM. 2020.

(60) Zumdahl, S.; Zumdahl, S.; DeCoste, D. *Chemistry*; 2017.

(61) U.S. Geological Survey. PHREEQC (Version 3) - A Computer Program for Speciation, Batch-Reaction, One-Dimensional Transport, and Inverse Geochemical Calculations.

(62) Kaiser, V.; Bramwell, S. T.; Holdsworth, P. C. W.; Moessner, R. Onsager's Wien Effect on a Lattice. *Nat. Mater.* **2013**, *12* (11), 1033–1037. https://doi.org/10.1038/nmat3729.

(63) Kaiser, V. The Wien Effect in Electric and Magnetic Coulomb Systems - from Electrolytes to Spin Ice. **2015**, 191.

(64) Newman, J.; Thomas-Alyea, K. E. *Electrochemical Systems*, 3rd ed.; John Wiley and Sons, Inc.: Hoboken, NJ, 2004.

(65) Onsager, L.; Fuoss, R. M. Irreversible Processes in Electrolytes. Diffusion, Conductance, and Viscous Flow in Arbitrary Mixtures of Strong Electrolytes. *J. Phys. Chem.* **1932**, *36* (11), 2689–2778. https://doi.org/10.1021/j150341a001.

(66) Divekar, A. G.; Antunes, C. M.; Yang-Neyerlin, A. C.; Pivovar, B. S. Understanding the Mass Transfer and Diffusion Effects of Carbon-Dioxide Absorption with Reaction in an Anion Exchange Membrane. **2019**.

(67) Berlinger, S. A.; McCloskey, B. D.; Weber, A. Z. Inherent Acidity of Perfluorosulfonic Acid Ionomer Dispersions and Implications for Ink Aggregation. *J. Phys. Chem. B* **2018**,

122 (31), 7790–7796. https://doi.org/10.1021/acs.jpcb.8b06493.

(68) Spry, D. B.; Fayer, M. D. Proton Transfer and Proton Concentrations in Protonated Nafion Fuel Cell Membranes. *J. Phys. Chem. B* **2009**, *113* (30), 10210–10221. https://doi.org/10.1021/jp9036777.

(69) Sondheimer, S. J.; Bunce, N. J.; Lemke, M. E.; Fyfe, C. A. Acidity and Catalytic Activity of Nafion-H. *Macromolecules* **1986**, *19* (2), 339–343. https://doi.org/10.1021/ma00156a016.

(70) Ehlinger, V. M.; Crothers, A. R.; Kusoglu, A.; Weber, A. Z. Modeling Proton-Exchange-Membrane Fuel Cell Performance/Degradation Tradeoffs with Chemical Scavengers. *J. Phys. Energy* **2020**.

(71) Grew, K. N.; Chiu, W. K. S. A Dusty Fluid Model for Predicting Hydroxyl Anion Conductivity in Alkaline Anion Exchange Membranes. *J. Electrochem. Soc.* **2010**, *157* (3), B327. https://doi.org/10.1149/1.3273200.

(72) Grew, K. N.; Ren, X.; Chu, D. Effects of Temperature and Carbon Dioxide on Anion Exchange Membrane Conductivity. *Electrochem. Solid-State Lett.* **2011**, *14* (12), 5–10. https://doi.org/10.1149/2.011112esl.

(73) Choi, P.; Jalani, N. H.; Datta, R. Thermodynamics and Proton Transport in Nafion II. Proton Diffusion Mechanisms and Conductivity. *J. Electrochem. Soc.* **2005**, *152* (3). https://doi.org/10.1149/1.1859814.

(74) Natzle, W. C.; Moore, C. B. Recombination of Hydrogen Ion (H+) and Hydroxide in Pure Liquid Water. *J. Phys. Chem.* **1985**, *89* (12), 2605–2612.

https://doi.org/10.1021/j100258a035.

(75) Critchfield, F. E.; Gibson, J. A.; Hall, J. L. Dielectric Constant for the Dioxane-Water System from 20 to 35°. *J. Am. Chem. Soc.* **1953**, *75* (8), 1991–1992. https://doi.org/10.1021/ja01104a506.

(76) Peng, J.; Roy, A. L.; Greenbaum, S. G.; Zawodzinski, T. A. Effect of CO2 Absorption on Ion and Water Mobility in an Anion Exchange Membrane. *J. Power Sources* **2018**, *380* (November 2017), 64–75. https://doi.org/10.1016/j.jpowsour.2018.01.071.

(77) Weber, A. Z.; Newman, J. Transport in Polymer-Electrolyte Membranes. *J. Electrochem. Soc.* **2004**, *151* (2), A311. https://doi.org/10.1149/1.1639157.

(78) Resasco, J.; Lum, Y.; Clark, E.; Zeledon, J. Z.; Bell, A. T. Effects of Anion Identity and Concentration on Electrochemical Reduction of CO2. *ChemElectroChem* **2018**, *5* (7), 1064–1072. https://doi.org/10.1002/celc.201701316.

(79) Larrazábal, G. O.; Strøm-Hansen, P.; Heli, J. P.; Zeiter, K.; Therkildsen, K. T.; Chorkendorff, I.; Seger, B. Analysis of Mass Flows and Membrane Cross-over in CO2 Reduction at High Current Densities in an MEA-Type Electrolyzer. *ACS Appl. Mater. Interfaces* **2019**, *11* (44), 41281–41288. https://doi.org/10.1021/acsami.9b13081.

(80) Sankir, M.; Kim, Y. S.; Pivovar, B. S.; McGrath, J. E. Proton Exchange Membrane for DMFC and H2/Air Fuel Cells: Synthesis and Characterization of Partially Fluorinated Disulfonated Poly(Arylene Ether Benzonitrile) Copolymers. *J. Memb. Sci.* **2007**, *299* (1–2), 8–18. https://doi.org/10.1016/j.memsci.2007.04.004.

(81) Wilhelm, F. G. *Bipolar Membrane Electrodialysis - Membrane Development and*

Transport Characteristics; 2001.

(82) Bazinet, L.; Lamarche, F.; Ippersiel, D. Bipolar-Membrane Electrodialysis: Applications of Electrodialysis in the Food Industry. *Trends Food Sci. Technol.* **1998**, *9* (3), 107–113. https://doi.org/10.1016/S0924-2244(98)00026-0.

(83) Balster, J.; Stamatialis, D. F.; Wessling, M. Electro-Catalytic Membrane Reactors and the Development of Bipolar Membrane Technology. *Chem. Eng. Process. Process Intensif.* **2004**, *43* (9), 1115–1127. https://doi.org/10.1016/j.cep.2003.11.010.

(84) Kushner, D. I.; Crothers, A. R.; Kusoglu, A.; Weber, A. Z. Transport Phenomena in Flow Battery Ion-Conducting Membranes. *Curr. Opin. Electrochem.* **2020**, *21*, 132–139. https://doi.org/10.1016/j.coelec.2020.01.010.

(85) Kreuer, K. D.; Paddison, S. J.; Spohr, E.; Schuster, M. Transport in Proton Conductors for Fuel-Cell Applications: Simulations, Elementary Reactions, and Phenomenology. *Chem. Rev.* **2004**, *104* (10), 4637–4678. https://doi.org/10.1021/cr020715f.

(86) Kreuer, K. D. The Role of Internal Pressure for the Hydration and Transport Properties of Ionomers and Polyelectrolytes. *Solid State Ionics* **2013**, *252*, 93–101. https://doi.org/10.1016/j.ssi.2013.04.018.